Majorana Loop Models for Measurement-Only Quantum Circuits

Kai Klocke[1] and Michael Buchhold[2]
[1]Department of Physics, University of California, Berkeley, California 94720, USA
[2]Institut für Theoretische Physik, Universität zu Köln, D-50937 Cologne, Germany

(Received 7 July 2023; revised 9 October 2023; accepted 13 October 2023; published 9 November 2023)

Projective measurements in random quantum circuits lead to a rich breadth of entanglement phases and extend the realm of nonunitary quantum dynamics. Here, we explore the connection between measurement-only quantum circuits in one spatial dimension and the statistical mechanics of loop models in two dimensions. While Gaussian Majorana circuits admit a microscopic mapping to loop models, for non-Gaussian, i.e., generic Clifford, circuits, a corresponding mapping may emerge only on a coarse-grained scale. We then focus on a fundamental symmetry of loop models: the orientability of worldlines. We discuss how orientability enters in the measurement framework, acting as a separatrix for the universal long-wavelength behavior in a circuit. When orientability is broken, the circuit falls into the universality class of closely packed loops with crossings (CPLC) and features a Goldstone phase with a peculiar, universal $\log^2(L)$ scaling of the entanglement entropy. In turn, when orientability is preserved, the long-wavelength behavior of the circuit mimics that of (coupled) two-dimensional Potts models. We demonstrate the strength of the loop model approach by numerically simulating a variety of measurement-only Clifford circuits. Upon varying the set of measured operators, a rich circuit dynamics is observed, ranging from CPLC to the one-state Potts model (percolation), the two-state Potts model (Ising), and coupled Potts models (Berezhinskii-Kosterlitz-Thouless) universality class. Loop models, thus, provide a handle to access a large class of measurement-only circuits and yield a blueprint on how to realize desired entanglement phases by measurement.

DOI: 10.1103/PhysRevX.13.041028 Subject Areas: Quantum Information, Statistical Physics

I. INTRODUCTION

Quantum circuits in the noisy intermediate-scale quantum (NISQ) era represent an exciting playground to explore novel types of quantum dynamics [1]. Recent examples range from testing elementary digital quantum computing algorithms, such as error correction [2–8] or topological state preparation [9–14], to the realization of nonequilibrium quantum many-body states without an equilibrium counterpart [15,16].

A particular role, unique to quantum circuits, is played by measurements. Evolution generated by measurement yields irreversible, nonunitary quantum dynamics, which provides *directionality* to a circuit. At the same time, measurements preserve the purity of a wave function. This enables a genuine quantum evolution, based only on the noncommutativity of operators, i.e., of the generators of the dynamics. Applying sequences of consecutive measurements, thus, provides the potential to implement new types of directional quantum dynamics in order to evolve and to prepare desired quantum many-body states in near-term NISQ devices. This prospect has led to fruitful activity among a broad, interdisciplinary research community. A prominent example for the novel type of quantum dynamics induced by measurement is measurement-induced phase transitions in the behavior of the entanglement entropy [17].

Entanglement transitions induced by measurements, competing with either unitary gates [18–40], Hamiltonian evolution [41–57], or other, incommensurate measurements [32,58–64], have advanced our understanding of nonunitary quantum dynamics and have established new links between research areas. Measurement-induced phase transitions have, for instance, been connected to quantum error correction [22,28,33,62], measurement-based quantum computation [64], quantum state preparation [65–67], and quantum teleportation [11,68], bridging quantum information science, where measurements traditionally play a vital role, with nonequilibrium physics and aspects of statistical mechanics, e.g., nonunitary conformal field theories.

Here, we undertake a closer inspection of one further interdisciplinary theme: the relation between $(1+1)$-dimensional measurement-only quantum circuits and two-dimensional (2D) loop models. Often admitting exact

treatment or efficient numerical simulation, loop models are a powerful tool for studying paradigmatic statistical mechanics models, such as Potts models and conformal field theory [69–72]. Since their introduction, loop models have enjoyed a long and rich history, touching many aspects of physics ranging from the classical statistical mechanics of polymers [73–77] and cosmic strings [78–82], to quantum Monte Carlo algorithms [83,84], Hall transitions [85–89], and magnetism [90–94], to knot invariants in topological quantum field theory [95–98]. In the past decade, there has been a renewed interest in better understanding universality classes which emerge from loop models subject to particular dynamical constraints or perturbations [92,95,99–108]. More recently, entanglement dynamics in a particular family of random Clifford circuits has been expressed in terms of Majorana fermion worldlines, making concrete connection to well-studied loop models [32,109–111]. In this work, we expand this connection between loop models and random Clifford circuits. We argue, based on general considerations, that a large class of both Gaussian and non-Gaussian measurement-only circuits can be understood in an (emergent) loop model framework. We confirm this perspective by performing numerical simulations for a set of measurement-only circuits.

First, we show how, in one dimension (1D), Gaussian Majorana projection operators and SWAP gates generate either the paradigmatic Temperley-Lieb (TL) or, more generally, the Brauer algebra. Consequently, any 1D circuit constructed from discrete, Gaussian operations admits a loop model representation. Based on the particular form of the algebra, we introduce a key concept for loop models and the corresponding circuits: the loop orientability.

Orientability is a hidden U(1) symmetry, which determines the long-wavelength behavior in the circuit. If present, the dynamics in the circuit are related to loop models without crossings, which can be furnished with a TL algebra, such as the 2D Potts model. When orientability is broken, however, the circuit approaches the long-wavelength behavior of a closely packed loop model with crossings (CPLC) [100]. The latter gives rise to an unconventional symmetry broken *Goldstone* phase with a characteristic $\sim \log^2(L)$ growth of the entanglement entropy. We show that, in a circuit, this symmetry has an interpretation in terms of both the circuit geometry and the form of the generators of the evolution: First, orientable circuits admit a *bipartition* of the underlying Majorana lattice such that only parities between different sublattices are measured. Second, this is equivalent of finding a representation of the circuit where all generators of the evolution obey *time-reversal symmetry*.

The latter provides an angle to extend the symmetry to non-Gaussian, i.e., generic, random Clifford, circuits. The measurement of operators that are even under time reversal preserves orientable structures, while measuring operators that are odd under time reversal breaks orientability. As a result, the former provides an interpretation of non-Gaussian measurement-only circuits in terms of coupled, i.e., *interacting*, Q-state Potts models, which may admit an exact analytical solution, while the latter pushes the circuit into a non-Gaussian CPLC.

We confirm this picture by numerically simulating measurement-only Clifford circuits with nearest- and next-nearest-neighbor qubit measurements. Whenever the measurements break orientability, in either the Gaussian or non-Gaussian case, we find that the long-wavelength behavior of the circuit is described by the CPLC. Depending on the set of performed measurements, the circuit realizes a set of topologically distinct area-law phases, which are separated from each other by an extended Goldstone phase. The Goldstone phase and its critical line are described by the CPLC nonlinear sigma model [100], or an enlarged supersymmetric field theory [112], yielding universal behavior for the entanglement growth, including the numerical prefactors, which are exactly recovered by the (non-)Gaussian circuits.

In turn, for the orientable nearest-neighbor circuits, we establish a direct connection to coupled one-state Potts models via the transfer matrix method and the Temperley-Lieb algebra. This provides an analytical approach to understand the rich phase diagram which arises in the orientable non-Gaussian model. Depending on the parameter regime, it realizes a series of measurement-induced phases and phase transitions: (i) a phase transition between topologically distinct area-law phases, which is described by the one-state Potts model (equivalent to 2D bond percolation); (ii) the branching of the one-state Potts model critical point into two Berezhinskii-Kosterlitz-Thouless (BKT) transitions, separated by an extended critical phase, which is described by two ferromagnetically coupled one-state Potts models; (iii) an emergent volume-law phase, where Majorana worldlines braid freely due to the competition between non-Gaussian measurements; and (iv) a novel measurement-induced phase transition separating two topologically distinct, non-Gaussian area-law phases, which is described by the Ising universality class of the two-state Potts model. We confirm these scenarios by matching the critical exponents ν, η, and $\eta_{\|}$ to the known values for Potts models.

The link to loop models, and the focus on orientability as a relevant symmetry, gives rise to a practical approach both to classify and to analytically solve many classes of measurement-only circuits. Furthermore, it provides a toolbox to realize desired loop model phases by implementing the corresponding classes of (non-)Gaussian measurements.

The paper is organized as follows. We begin in Sec. II by reviewing fundamental aspects of loop models in two spatial dimensions (2D) and by linking them to the dynamics in $(1+1)$-dimensional measurement-only Clifford circuits. In Sec. II A, we give a concrete mapping

between Gaussian Majorana circuits and 2D loop models, and we discuss the loop model observables in Sec. II B. We then introduce the notion of worldline orientability and its role in classifying measurement-only circuits in Sec. II C. We conclude this section by examining the robustness of the loop model picture when including non-Gaussian measurements in Secs. II E and II F.

In Sec. III, we examine a set of (non-)Gaussian measurement-only circuits for nearest-neighbor and next-nearest-neighbor Pauli measurements. We separate the circuits by symmetry into orientable and nonorientable ones, and we validate their anticipated behavior based on symmetry. In Sec. III A (III B), we explore Gaussian (non-Gaussian) orientable circuits and argue that their behavior can be understood in the framework of coupled 2D Potts models. In Sec. III C (III D), we, in turn, explore Gaussian (non-Gaussian) nonorientable circuits, and we show that in both cases they realize a CPLC Goldstone phase with universal properties. In Sec. IV, we discuss spacetime duality for Majorana circuits, and we argue that the measurement-only phases discussed in this work do not have a purely unitary spacetime dual counterpart. Finally, we consider the measurement-only $XZZX$ quantum code in Sec. V and argue, based on geometry, that it is generally nonorientable and that it realizes a CPLC Goldstone phase.

II. FROM 1D QUBIT CIRCUITS TO 2D LOOP MODELS

We consider measurement-only circuits of L qubits, which are arranged in a one-dimensional chain. By virtue of the Jordan-Wigner (JW) transformation, such circuits may be represented in terms of Majorana fermions, including in the presence of parity-violating measurements. We argue, and subsequently numerically confirm, that this further enables a mapping of the circuit to the statistical mechanics of completely packed (dense) loop models in 2D [77,112–116]. For Gaussian Majorana operations, i.e., quadratic in Majorana fermions, this mapping is exact on the level of the microscopic circuit. For non-Gaussian circuits, the loop model is emergent and may depend on the complete set operators that is measured and on the parameter regime.

In this section, we discuss the mapping of Majorana circuits to loop models based on (i) the TL and Brauer algebras [117] and (ii) the worldlines for the Majoranas. We then discuss a central aspect of these loop models: the orientability of Majorana worldlines. The presence or absence of orientability leads to fundamentally different long-wavelength physics realized in the circuit. We, thus, separate measurement-only circuits in the following discussion into orientable and nonorientable. Orientable models can be studied by a number of well-established techniques ranging from the TL representation of the transfer matrix to Coulomb gas approaches. In contrast, nonorientable loop models generically yield nonplanar worldline configurations, termed CPLC, which cannot be expressed by an element of the TL algebra. As one major consequence, they allow for a nonunitary symmetry-broken phase in two dimensions, the *Goldstone phase* of the CPLC [100,112].

We proceed in this section by including non-Gaussian measurements. We focus on two aspects: the relevance in the renormalization group sense and the impact on the orientability of the loop model representation.

A. Mapping discrete Gaussian Majorana circuits to loop models

Here, we introduce the mapping between the statistical mechanics of two-dimensional loops and the dynamics of $(1+1)$-dimensional, discrete Gaussian Majorana circuits. We label the L qubits in the circuit by an index $j = 1, \ldots, L$. Each qubit j admits an alternative representation in terms of two Majorana fermions γ_{2j-1} and γ_{2j}, which fulfill the anticommutation relation $\{\gamma_l, \gamma_m\} = 2\delta_{l,m}$ for $l, m = 1, \ldots, 2L$. The circuit evolves under measurements of Pauli strings $\hat{O}$; i.e., each operator $\hat{O}$ is a string $\hat{O} = \bigotimes_{j=1}^{L} \hat{A}_j$ with $\hat{A}_j \in \{\mathbb{1}_j, X_j, Y_j, Z_j\}$ being a Pauli operator or the identity acting on qubit j.

Under the JW transformation, each Pauli string yields a corresponding Majorana operator which falls into one of three categories: (i) *Gaussian* operators $\hat{O} = i\gamma_l\gamma_m$ consisting of exactly two Majorana modes, (ii) parity-preserving but non-Gaussian operators $\hat{O} = i^n \prod_{l=1}^{n>1} \gamma_{j_{2l-1}}\gamma_{j_{2l}}$ consisting of an even number of Majorana modes, and (iii) parity-breaking operators $\hat{O} = \gamma_{j_{2l+1}} i^n \prod_{l=1}^{n\geq 0} \gamma_{j_{2l-1}}\gamma_{j_{2l}}$ consisting of an odd number of Majorana modes.

We start with the Gaussian case, i.e., $\hat{O} = i\gamma_l\gamma_m$, and introduce the projector $\mathcal{P}_{lm} \equiv \frac{1}{2}(\mathbb{1} + \hat{O}) = \frac{1}{2}(\mathbb{1} + i\gamma_l\gamma_m)$ onto the positive measurement outcome $\hat{O} = +1$. The opposite outcome is obtained by exchanging $l \leftrightarrow m$. Similarly, we introduce the unitary $\mathcal{R}_{lm} \equiv \exp[i(\pi/4)\hat{O}] = (1/\sqrt{2})(\mathbb{1} - \gamma_l\gamma_m)$, which swaps Majoranas $\gamma_l \leftrightarrow \gamma_m$. Upon normalization of the state after each projection, for four different Majorana fermions γ_n, γ_s, γ_l, and γ_m, this yields the algebra

$$0 = [\mathcal{P}_{lm}, \mathcal{P}_{ns}] = [\mathcal{R}_{lm}, \mathcal{R}_{ns}], \tag{1}$$

$$\mathcal{P}_{lm} = \mathcal{P}_{lm}^2 = \mathcal{P}_{lm}\mathcal{P}_{nl}\mathcal{P}_{lm}, \tag{2}$$

$$\mathcal{P}_{lm} = \mathcal{R}_{ms}^\dagger \mathcal{P}_{ls}\mathcal{R}_{ms}, \qquad \mathcal{R}_{lm} = \mathcal{R}_{ms}^\dagger \mathcal{R}_{ls}\mathcal{R}_{ms}, \tag{3}$$

$$\mathcal{R}_{lm}^4 = \mathbb{1}. \tag{4}$$

We emphasize that the last equality in Eq. (2) is not an operator identity (which would require a factor $\frac{1}{2}$) but holds when the quantum state on which the projectors are acting is normalized after each measurement.

The algebra is general and holds for any combination of Majorana indices. If we restrict the projectors $\mathcal{P}_{lm}$ to nearest-neighbor pairs $|l-m|=1$ and exclude swaps, then Eqs. (1) and (2) yield the paradigmatic TL algebra. The TL algebra describes families of exactly solvable loop models, here with loop fugacity $n=1$, such as the one-state Potts model [71,118]. If we include nearest-neighbor swaps $\mathcal{R}_{lm}$ with $|l-m|=1$, Eqs. (1)–(3) reveal yet another loop model structure, known as the Birman-Murakami-Wenzl (BMW) algebra [106,119–121].

Importantly, lifting the constraint $|l-m|=1$ and allowing measurements and swaps $\mathcal{P}_{lm}$ and $\mathcal{R}_{lm}$ of arbitrary Majorana pairs γ_l and γ_m, all operations remain well described by the BMW algebra. By virtue of Eq. (3), any nonlocal swap $\mathcal{R}_{lm}$ or measurement $\mathcal{P}_{lm}$ with $|l-m|>1$ can be expressed via a sequence of nearest-neighbor swaps, e.g., $\mathcal{P}_{1,3}=\mathcal{R}_{2,3}^{\dagger}\mathcal{P}_{1,2}\mathcal{R}_{2,3}$. The BMW algebra, thus, provides a framework for arbitrary measurement-only circuits of Gaussian Majorana operators $\hat{O}=i\gamma_l\gamma_m$.

Dense loop models naturally correspond to diagrammatic representations of the TL or BMW algebra, which for Gaussian Majorana circuits are quite intuitive. The instantaneous quantum state of a Gaussian Majorana circuit at each point in time is characterized by the fermion parities $\langle i\gamma_l\gamma_m\rangle=0,\pm1$. It is represented by a free-fermion stabilizer state

$$\rho=\prod_l\frac{1}{2}(1-i\gamma_{l_1}\gamma_{l_2}), \tag{5}$$

where l labels all the Majorana pairs with mutually well-defined parity $|\langle i\gamma_{l_1}\gamma_{l_2}\rangle|=1$. For a pure state with $2L$ Majorana fermions, there are L such pairs, while their number is less if the state is mixed. Diagrammatically, we can represent the state ρ by drawing a worldline for each Majorana and connecting the worldlines of each pair l_1, l_2 through an open arc. Evolving ρ under the circuit dynamics, the Majorana pairings are rearranged, which is reflected by scrambled pairings of worldlines in the $(1+1)$-dimensional spacetime lattice, as shown in Fig. 1(b).

For each time step t and neighboring pair l, m on the tilted square (brick-wall) lattice, one of the following generators of the BMW algebra is applied, as shown in Fig. 1(a). The identity $\mathbb{1}_{lm}$ leaves the pairings unmodified, and so diagrammatically it propagates Majorana fermions γ_l and γ_m in time. A swap $\mathcal{R}_{lm}$ exchanges Majoranas $\gamma_l\leftrightarrow\gamma_m$ such that the corresponding worldlines cross over one another. A parity measurement $\mathcal{P}_{lm}$ takes initial pairings $\gamma_k\gamma_l$ and $\gamma_m\gamma_n$ and yields a state with pairings $\gamma_l\gamma_m$ and $\gamma_k\gamma_n$. To achieve such a rearrangement, the loop end points at l and m are fused to give a single arc connecting γ_k and γ_n. Then a new arc is drawn between γ_l and γ_n. The resulting operation can be viewed as propagating loops in the spatial direction. See Fig. 2 for a

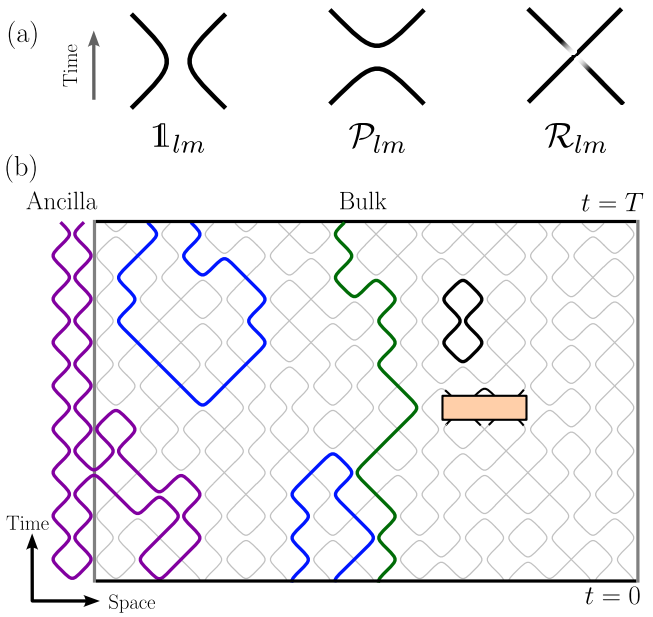

FIG. 1. Loop representation of Gaussian Majorana circuits. (a) The three elementary operations on a pair of Majorana worldlines: The identity $\mathbb{1}_{lm}$ propagates unaffected loops in the temporal direction. A projective parity measurement $\mathcal{P}_{lm}$ connects loops in the opposite way, appearing like spatial propagation. A swap gate $\mathcal{R}_{lm}$ makes the worldlines cross over one another. (b) A loop configuration for brick-wall Majorana circuit of depth T. Different types of loops contribute to different correlation functions: Spanning loops (green) connect the two temporal boundaries, fixing boundary correlation functions like $\langle\gamma_i(t=0)\gamma_j(t=T)\rangle$. Loops with both ends terminating on the same temporal boundary (blue) determine the equal-time spatial correlations $\langle\gamma_i(t)\gamma_j(t)\rangle|_{t=0,T}$. Adding ancilla Majorana modes allows loops (purple) to cross the spatial boundaries. Closed loops (black) contained entirely in the spacetime bulk do not contribute to boundary observables but modify bulk correlation functions. Non-Gaussian, e.g., four-fermion, measurements are represented as multileg vertices (orange box) which are not immediately expressed as a single loop configuration.

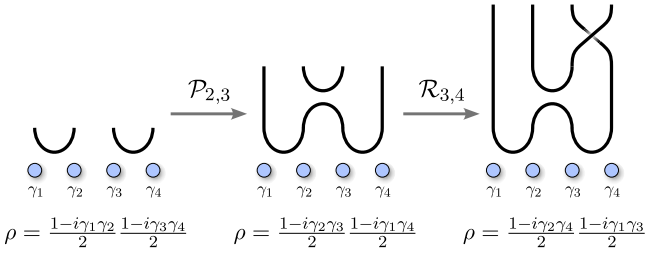

FIG. 2. Diagrammatic representation of a Majorana stabilizer state and its evolution under the Gaussian circuit dynamics. The instantaneous state ρ is specified by pairs of Majoranas corresponding to the end point open arcs in the diagram. Measurement $\mathcal{P}_{2,3}$ can be represented by fusing the loop end points at γ_2 and γ_3 and opening a new arc to produce the pairings in the postmeasurement state. A swap gate $\mathcal{R}_{3,4}$ is represented by a loop crossing which exchanges γ_3 and γ_4.

minimal example of how the loop representation of the state evolves under such operations.

A selection of possible spacetime loops, including potential boundary conditions, is shown Fig. 1(b). As one infers from the diagrams, the loop representation makes no distinction between $\mathcal{P}_{lm}$ and $\mathcal{P}_{ml}$; i.e., it is agnostic to the sign of each parity measurement outcome. Thus, each loop diagram represents an equivalence class of circuits rather than a specific circuit realization. Each circuit of a given equivalence class is identical up to the random measurement outcomes and the sign of the swap gates. Consequently, each equivalence class predicts quantities that are independent of measurement outcomes. Examples include the modulus $|i\langle\gamma_l\gamma_m\rangle| = 0,\ 1$ of each parity, the entanglement entropy, and the purity of the state.

This equivalence relation identifies both signs of swap gates $\mathcal{R}_{lm} \sim \mathcal{R}_{lm}^\dagger$ such that Eq. (4) is replaced by $\mathcal{R}_{lm}^2 \sim \mathbb{1}$. Then the relation between the operations reduces to the Brauer algebra, i.e., the degenerate point of the BMW algebra. The Brauer algebra $\mathcal{B}_N$ consists of pairwise matchings between $2N$ elements, which we can identify with the end points of Majorana worldlines at temporal boundaries of the circuit. Then the elements of $\mathcal{B}_N$ are in one-to-one correspondence with equivalence classes of Gaussian Majorana circuits, specified by the pairings $|i\langle\gamma_l\gamma_m\rangle|$. Two circuits from the same equivalence class can be transformed into one another by applying a series of local phase gates, which do not change the entanglement. This is true for general Clifford circuits [122] and enables an experimental procedure to detect the predicted observables [15].

B. Circuit observables and loop configurations

The dynamics of a circuit are characterized by bulk and boundary observables. The latter are correlations at the temporal boundary, i.e., in the final state $\rho(T)$, such as the entanglement entropy. When the circuit has a rigorous loop model representation, $\rho(T)$ can be inferred from boundary loop configurations. Then it is more efficient to simulate the corresponding loop model rather than the Clifford circuit (see Appendix A for details). When no such microscopic mapping to a loop model is possible, we instead simulate the Clifford circuit via the tableau formalism [123]. Below, we provide a dictionary connecting observables in Clifford circuits and in loop models.

We begin with two paragraphs providing a short summary of Clifford circuits and the stabilizer formalism. A generic stabilizer state, emerging from a non-Gaussian Clifford circuit, is a generalization of Eq. (5) to Pauli operators that are not quadratic in Majorana fermions. It can be written as a product of commuting projectors: $\rho = \prod_{i=1}^{|\mathcal{G}|} \frac{1}{2}(1 - M_i)$, where M_i are linearly independent Pauli strings satisfying $[M_i, M_j] = 0$. The set $\mathcal{G} = \{M_i\}$ generates the stabilizer group $\mathcal{S} = \langle\mathcal{G}\rangle$ for the state ρ. Such states admit an efficient representation in the tableau formalism wherein the only Pauli strings and phases for stabilizer group generators M_i are recorded [123,124]. Under the action of Clifford operations, the M_i are transformed into new Pauli strings, ensuring the continued existence of a compact representation and enabling a fast update of the tableau. Similarly, projective measurement of a Pauli string $\tilde{M}$ can be simulated in polynomial time in the following manner. Suppose we order the stabilizer generators $\langle M_1, \ldots, M_i, M_{i+1}, \ldots\rangle$ such that $[M_j, \tilde{M}] = 0$ for $j < 0$ and $\{M_j, \tilde{M}\} = 0$ for $j \geq i$. The postmeasurement state can be represented by the new stabilizer generators $\langle M_1, \ldots, \tilde{M}, M_i M_{i+1}, \ldots\rangle$.

Given a stabilizer state, the entanglement entropy of subsystem A is given by $S_A = \dim_{\mathbb{F}_2}(\mathcal{G}|_A) - |A|$ [122], where $\mathcal{G}|_A$ is the restriction of the tableau to subsystem A and the rank is taken with respect to $\mathbb{F}_2$. Similarly, the residual entanglement of a mixed state on L qubits is given by $|\mathcal{G}| - L$. Further entanglement measures such as mutual information may be obtained by such a calculation on the appropriate subsystems.

In a loop model, boundary observables are encoded in the distribution of fermion parities $|\langle\gamma_m\gamma_l\rangle_T|$ at time T. Each nonzero parity corresponds to a loop arc connecting sites l and m with the length of the arc defined as $\ell = |l - m|$ [125]. The entanglement properties and correlations in $\rho(T)$ are captured by the normalized loop length distribution $P(\ell)$, which is in one-to-one correspondence with the stabilizer length distribution in the clipped gauge [26,104]. At a critical point of the loop model, the loop length distribution takes the form $P(\ell) = \tilde{c}(\ell)[3\log(2)/\ell^2]$ with a universal prefactor $\tilde{c}(\ell)$. In Table I, we show the known values of $\tilde{c}(\ell)$ for both CPLC and the Q-state Potts model.

1. Entanglement entropy and mutual information

From the state $\rho(T)$, we compute the von Neumann entanglement entropy $S_A \equiv -\mathrm{Tr}[\rho_A(T)\log_2\rho_A(T)]$ of a subregion A and the mutual information $I_2(A,B) \equiv S_A + S_B - S_{AB}$ between two subregions A and B. Here, $\rho_A(T) = \mathrm{Tr}_{\bar{A}}[\rho(T)]$ is the reduced density matrix obtained by tracing

TABLE I. Asymptotic behavior of the loop length distribution for the long-loop phases of CPLC and the critical point of the Q-state Potts models. It determines the prefactor of the von Neumann entanglement entropy $S_{L/2} = [\tilde{c}(L)/3]\log(L)$.

State	$\ell^2 P(\ell)\left[\frac{1}{3\log(2)}\tilde{c}(\ell)\right]$
Critical Q-state Potts [126]	$\frac{(2+\sqrt{Q})}{\pi\sqrt{4-Q}}\frac{\mathrm{arcsec}(2/\sqrt{Q})}{\mathrm{arcsec}(-2/\sqrt{Q})}$
CPLC critical point [100]	$\frac{2.035}{\pi}$
CPLC Goldstone phase [100]	$\frac{1}{2\pi^2}\log(l) + \mathrm{const}$

out the complement $\bar{A}$ of A. In a Gaussian circuit, both S_A and $I_2(A,B)$ are determined by the set of fermion parities $|\langle\gamma_l\gamma_m\rangle_T| = 1$, i.e., by the loop arcs at $t = T$. Then $S_A = N_A$ [127] is the number of arcs N_A that terminate with one end in A and with the other end in its complement $\bar{A}$ [32,59,122]. For a loop distribution $P(\ell)$ with scaling $\ell^2 P(\ell) = 3\log(2)\tilde{c}(\ell)$ as in Table I, this is $N_A = \tilde{c}(|A|)/3\log(2)$ (see Appendix A). The mutual information $I_2(A,B)$ is twice the number of loops with one end point in A and the other end point in B. For Gaussian circuits and loop models, mutual information is additive; i.e., $I_2(A,BC) = I_2(A,B) + I_2(A,C) - I_2(A,B\cap C)$ [128].

In order to detect long-range entangled states in the circuit of $2L$ fermions, we compute the mutual information between contiguous subsystems A and B of size $|A| = |B| = L/4$ Majorana fermions with separation $L/4$ (e.g., $A = [1, L/4]$ and $B = [L/2+1, 3L/4]$). For this choice, $I_2(A,B)$ provides a convenient metric for the finite-size scaling analysis in the vicinity of a critical point. It can be used for both locating an entanglement transition and determining the critical exponent ν [129,130].

2. Multipartite entanglement

For a Gaussian circuit, i.e., for loop models, every open loop has precisely two end points [32] and zero operator content between them. Thus, any multipartite entanglement can be expressed by the sum of bipartite mutual information. For instance, the tripartite mutual information $I_3(A,B,C)$ always vanishes in a loop model. This is different for generic Clifford circuits: While for contiguous and adjacent subsystems A and B the entanglement entropy of a stabilizer state is the same as for the corresponding Majorana wave function, this is no longer true when computing the mutual information between *disconnected* regions [131].

3. Purity and erasure of initial information

For a circuit with Majorana worldline representation, the *spanning number* $n_s(T)$ counts the number of worldlines connecting the $t = 0$ and $t = T$ temporal boundaries of the circuit. It is the mutual information between the initial and the final state and, thus, quantifies the survival of information inserted into the circuit at $t = 0$ up to the final time $t = T$. We distinguish two important cases: First, when the initial state is maximally mixed, it hosts only unpaired Majorana worldlines, and the spanning number counts all unpaired Majorana worldlines at time T. This provides the total entropy $S_L(T) = -\mathrm{Tr}[\rho(T)\log_2\rho(T)] = \frac{1}{2}n_s(T)$, i.e., the time-dependent purity. Second, when the initial state is pure, $n_s(T)$ is the number of Majorana parities which have not been erased by measurements. Then it measures the survival probability of initially encoded information. This elucidates the equivalence between dynamical purification of an initial mixed state and the erasure of information from an initial pure state by measurement.

4. Bulk observables

Both 2D loop models and $(1+1)$D circuits hold information that is not accessible from boundary correlations. In loop models, an important example is the so-called watermelon correlator $G_{2n}(\vec{z},\vec{z}')$. For any integer n, it is the probability that the (two-dimensional) coordinates $\vec{z},\vec{z}'$ in the bulk of the loop configuration are connected by n *closed loops*. In the circuit $\vec{z} = (l,t)$, $\vec{z}' = (l',t')$ become spacetime coordinates and, e.g., $G_2(\vec{z},\vec{z}')$ is the probability that the two Majorana fermions γ_l and $\gamma_{l'}$ share the same worldline for intermediate times $0 < t, t' < T$ and $t \neq t'$. We express this as the parity $|\langle\gamma_l(t)\gamma_{l'}(t')\rangle| = 1$, which takes the form of an out-of-time order correlator. It reveals information about the dynamics that boundary correlations cannot access. In Appendix E, we show how this bulk quantity can be extracted from Gaussian and general Clifford circuits.

C. Worldline orientability, bipartite lattices, and time-reversal symmetry

A core aspect of the statistical mechanics of loop models and of measurement-only circuits is the so-called orientability of the loops. Orientability implies the presence of a continuous U(1) symmetry in the circuit, which determines its long-wavelength behavior. Consider a circuit of N Majorana fermions. We call this circuit and its corresponding loop model orientable if and only if there exists a bipartition A, B of the set of Majorana fermions such that (i) each measurement $\mathcal{P}_{l,m}$ connects exactly one Majorana $\gamma_l \in A$ and one Majorana $\gamma_m \in B$, (ii) each swap $\mathcal{R}_{l,m}$ acts on two Majoranas, which are either both in A, $\gamma_l, \gamma_m \in A$ or both in B, $\gamma_l, \gamma_m \in B$. In this case, loop configurations are elements of the *walled* Brauer algebra $\mathcal{B}_{|A|,|B|} \subset \mathcal{B}_N$ [132,133]. When no such bipartition exists, we call the circuit nonorientable. This provides a practical criterion for orientability in a loop model. If all (any) closed loops [see black configuration in Fig. 1(b)] originate from an even (odd) number of measurements, the circuit is bipartite (nonbipartite).

In an orientable circuit, we may label each Majorana worldline with an arrow denoting an orientation. Each worldline corresponding to subsystem A obtains a positive orientation (travels forward in time), and each worldline corresponding to subsystem B obtains a negative orientation (travels backward in time) [77]. Then the total orientation $Q = |A| - |B| \in \mathbb{Z}$ is a conserved charge with $-N \leq Q \leq N$. For a purely algebraic definition of the orientability symmetry operator, one may examine the group center of the walled Brauer algebra [132,133].

To elucidate the notion of orientability, consider the particular case of nearest- and next-nearest-neighbor measurements $\mathcal{P}_{l,l+1}$ and $\mathcal{P}_{l,l+2}$. With only nearest-neighbor measurements, we may take $A = \{\gamma_{2l-1}\}$ and $B = \{\gamma_{2l}\}$. As shown in Fig. 3(a), a measurement $\mathcal{P}_{l,l+1}$ preserves the

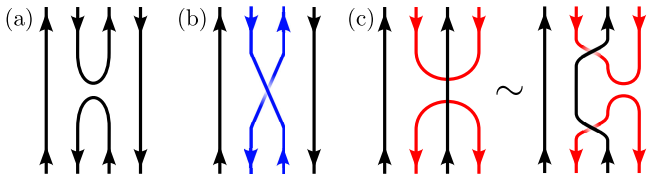

FIG. 3. Orientability of worldlines. Worldlines get assigned a fixed orientation for the even or the odd sublattice. (a) Nearest-neighbor measurements preserve this orientation. By contrast, (b) nearest-neighbor crossings and (c) next-nearest-neighbor measurements mix the orientations and break the associated symmetry.

orientations. In this particular example, the orientable charge appears reminiscent of a staggered "magnetization" of worldlines. To see this, we may map the circuit to the six-vertex model and obtain an explicit XXZ matrix representation of the TL generators [118,134,135]:

$$\mathcal{P}_{l,l+1} \to \frac{1}{2}\left[X_l X_{l+1} - Y_l Y_{l+1} + (Z_l Z_{l+1} + \mathbb{1})e^{\pm(i\pi/3)Z_l}\right],$$

where the phase in the exponential alternates between the sublattices. Here, the spin-1/2 degree of freedom for each worldline can be interpreted as the orientation of the loop. The U(1) orientability charge is then given by $Q = \sum_l (-1)^l Z_l$. Next-nearest-neighbor measurements, by contrast, act on two Majoranas lying on the same sublattice and are, thus, incompatible with the orientations [see Fig. 3(c)]. Moreover, the matrix representation for $P_{l,l+2}$ obtained by conjugating with swap gates does *not* commute with Q and so breaks the U(1) symmetry.

Furthermore, this example identifies orientability as the circuit counterpart of time-reversal symmetry in Majorana Hamiltonians. To see this, we first realize that a projection $\mathcal{P}_{l,l+m} = \frac{1}{2}(\mathbb{1} + i\gamma_l\gamma_{l+m})$ with m odd always connects a Majorana with an even index to a Majorana with an odd index. By convention, odd Majoranas are real $\gamma_{2l-1} \sim c_l^\dagger + c_l$, while even Majoranas are complex $\gamma_{2l} \sim i(c_l^\dagger - c_l)$. Thus, products $i\gamma_l\gamma_{l+m}$ with m odd are real and invariant under time reversal. The same is true for swaps $\mathcal{R}_{l,l+m} = (1/\sqrt{2})(\mathbb{1} - \gamma_l\gamma_{l+m})$, where for m even the product $\gamma_l\gamma_{l+m}$ is real. When all the generators of the evolution are invariant under time reversal, so is the entire circuit. The symmetry implies that all circuit observables that are odd under time reversal must have zero expectation value.

This framework can be further generalized: A given circuit has a time-reversal invariant representation and it preserves orientability whenever we can find a satisfactory bipartition A, B. This provides the equivalence of (i) the bipartiteness of a Majorana circuit, (ii) time-reversal invariance of the generators $\mathcal{P}$ and $\mathcal{R}$, and (iii) orientability of the corresponding loop model.

D. Effective long-wavelength description

Unambiguously mapping a monitored circuit to a loop model gives rise to a large toolbox of theoretical methods to examine its long-wavelength behavior. An important example is the mapping of dense loops to nonlinear sigma models (NLσMs) [100,112,113], whose form and universal behavior depend explicitly on the presence or absence of orientability. When the local orientations are conserved, the order parameter takes values in $\mathbb{CP}^{n-1}$. If, instead, orientability is broken, as in CPLC, the order parameter is reduced to $\mathbb{RP}^{n-1}$ [100]. The relevant case of $n = 1$ may be studied as a replica-like limit of the $n > 1$ theory [136].

Once orientability is broken sufficiently strongly, the corresponding NLσM features a phase transition from a short-loop phase to a symmetry-broken, so-called Goldstone phase. It is an order-disorder transition driven by $\mathbb{Z}_2$ vortex proliferation in the $\mathbb{RP}^{n-1}$ theory [100,112,113]. Despite taking place in two dimensions, this transition and the CPLC Goldstone phase are not prohibited by the Mermin-Wagner theorem, since a non-Hermitian representation is required for treating the $n = 1$ loop model [100,112]. Whenever orientability is broken in the circuit, we resort to the CPLC nonlinear sigma model results, which are universally confirmed in this case.

E. Symmetry-preserving non-Gaussian perturbations

The mapping of Gaussian Majorana circuits to loop models was based on the TL and Brauer algebra in Eqs. (1)–(3), which is rigorous for Gaussian circuits. We show below that measuring non-Gaussian operators creates superpositions of loop configurations. This is analogous to Hamiltonian systems, where interactions create superpositions of Gaussian states. In many situations, however, a unique loop model may emerge on a coarse-grained scale. Here, we adopt a perspective inspired by the renormalization group (RG) framework and consider measurements of non-Gaussian operators $\{\hat{O}_l\}$ as perturbations on top of an otherwise Gaussian circuit. We note that this situation is quite general: The frustration graph of an arbitrary set of measured operators always contains a subgraph that can be represented by measurements of Gaussian fermion operators [137]. The remaining operators then act as non-Gaussian perturbation.

Starting from a Gaussian circuit, i.e., a well-defined 2D loop model, the notion of relevance and irrelevance in the RG sense for non-Gaussian perturbations in 2D statistical mechanics is applicable. Thus, measuring a set of non-Gaussian operators $\{\hat{O}_l\}$, which preserve the symmetries of the Gaussian circuit, is an irrelevant perturbation when added to an extended thermodynamic phase of either short or long loops. The situation may, however, be different at a Gaussian critical point. Here, we distinguish relevant and irrelevant non-Gaussian operators, in analogy to

equilibrium statistical mechanics. Irrelevant operators do not modify the critical behavior at the fixed point when added only weakly, i.e., with small measurement probability. They might, however, drive a phase transition into a non-Gaussian phase once they start to dominate the circuit evolution, i.e., once their measurement probability is sufficiently large. This scenario is analogous to a strong-coupling fixed point in the renormalization group picture. In turn, relevant non-Gaussian operators would modify the critical behavior even when added only with small probability, similar to the Wilson-Fisher scenario: The Gaussian fixed point becomes repulsive and the critical behavior is determined by a different, interacting fixed point [138–141]. In this work, we do not observe the latter scenario.

The effect of symmetry-preserving non-Gaussian measurements in a loop model can be illustrated by starting with a Gaussian circuit described by the Brauer algebra in Eqs. (1)–(3). It is perturbed by measurements of non-Gaussian operators which are symmetry preserving, e.g., preserve parity and orientability and are, thus, even under time reversal. Let us take, for example, four-fermion parity checks, such as $Z_l Z_{l+1} = \gamma_{2l-1}\gamma_{2l}\gamma_{2l+1}\gamma_{2l+2}$ or $X_l X_{l+2} = \gamma_{2l}\gamma_{2l+1}\gamma_{2l+2}\gamma_{2l+3}$. The projective measurement $\mathcal{P}_{1,2,3,4} = \frac{1}{2}(\mathbb{1} - \hat{O}_{1,2,3,4})$ of a general four-fermion operator $\hat{O}_{1,2,3,4} = \gamma_1\gamma_2\gamma_3\gamma_4$ corresponds to an "eight-leg vertex" in the loop model. It has four incoming and four outgoing worldlines [see Fig. 4(a)], which, in contrast to two-fermion measurements, have *no* unambiguous connection between individual pairs of fermions. Instead, $\mathcal{P}_{1,2,3,4}$ yields a superposition of all possible ways of connecting the legs incident on the vertex with a fixed total parity. This gives rise to several, equivalent representations of $\mathcal{P}_{1,2,3,4}$ in the loop framework. For instance, the projector can be written as

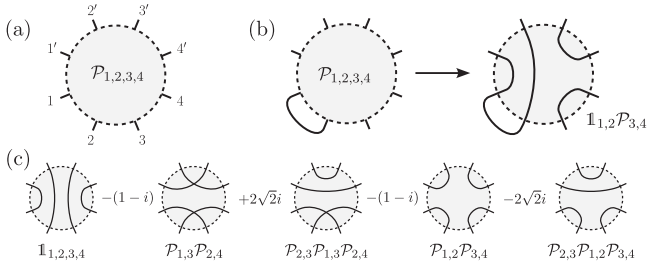

FIG. 4. Four-fermion measurements. (a) Measuring the total parity on four Majoranas γ_l for $l = 1, 2, 3, 4$ can be represented by an eight-leg vertex, where the unprimed and primed indices denote incoming and outgoing worldlines, respectively. (b) When one of the local fermion parities is known due to a closed loop entering the vertex, the measurement reduces to a parity check on two fermions, restoring a vertex-free loop diagram. (c) Without knowledge of the local parities, the vertex represents a sum over possible pairings of the legs. One of several equivalent diagrammatic representations is shown here. Notably, the sum includes configurations which are inconsistent with orienting the worldlines.

$$\mathcal{P}_{1,2,3,4} = \mathbb{1} - i\sqrt{2}\left(e^{-i\pi/4}\mathbb{1} - \sqrt{2}\mathcal{P}_{2,3}\right)\mathcal{P}_{1,3}\mathcal{P}_{2,4} + i\sqrt{2}\left(e^{+i\pi/4}\mathbb{1} - \sqrt{2}\mathcal{P}_{2,3}\right)\mathcal{P}_{1,2}\mathcal{P}_{3,4}. \quad (6)$$

The corresponding superposition of loop configurations is shown in Fig. 4(c). So far, the sum is *not* restricted to terms which respect the symmetry, e.g., orientability, of the Gaussian circuit and so may include both symmetry-preserving and symmetry-breaking terms.

We may now ask what the action of Eq. (6) will be in an otherwise Gaussian circuit. Whenever the parity of two of the four fermions is already known *or* measured in the future, the four-fermion measurement reduces to a two-fermion parity check, as revealed from $\mathcal{P}_{1,2}\mathcal{P}_{1,2,3,4} = \mathcal{P}_{1,2,3,4}\mathcal{P}_{1,2} = \mathcal{P}_{1,2}\mathcal{P}_{3,4}$ and depicted in Fig. 4(b). This provides access to two important limits: (i) When the circuit is dominated by local Gaussian measurements, an extensive number of local parities is known immediately before or after application of $\mathcal{P}_{1,2,3,4}$. Then $\mathcal{P}_{1,2,3,4}$ can almost always be replaced by two-fermion measurements. (ii) In turn, when non-Gaussian measurements are dominant, few Gaussian parity checks induce a cascade of fixed local parities, which collapses the circuit onto a short-loop state. Both cases give rise to a loop model interpretation, in which the topology of the short-loop (area-law) phase depends on (i) the Gaussian or (ii) the non-Gaussian measurements.

This observation is readily generalized to measurements of arbitrary symmetry-preserving Majorana operators $\hat{O} \sim \gamma_1, \ldots \gamma_{2n}$ with $n > 2$. When the parity of m bilinears in $\hat{O}$ is known, then it reduces to the measurement of an $2(n-m)$ Majorana operator. The size of the reduced operator corresponds precisely to the mutual information between the support of $\hat{O}$ and its complement in the circuit. This mutual information is a reliable indicator of the relevance of a $2n$-fermion operator in a Gaussian circuit. In an area-law phase with short loops, and for contiguous support of $\hat{O}$, it does not grow with n. At a critical point with long loops (logarithmic entanglement growth), it grows $\sim \log(n)$, such that higher-order operators become increasingly relevant. In this case, the $2n$-fermion measurements do not collapse onto a single loop configuration but, instead, yield a superposition of all symmetry-allowed configurations.

A further important consequence of the above discussion is that symmetry-preserving non-Gaussian measurements indeed inherit the symmetry of the Gaussian circuit. Consider, for instance, orientability: When the worldlines entering the $2n$-fermion vertex form an orientable, bipartite lattice, the corresponding vertex is collapsed onto its bipartite part and cannot break orientability. In turn, when the worldlines instead form a nonbipartite lattice, the $2n$-fermion vertex collapses onto its nonorientable part. Thus, $2n$-fermion parity checks, which are compatible with

orientability, i.e., even under time reversal, inherit the (non) orientable structure of the underlying Gaussian circuit.

F. Parity-violating measurements

A second important class of non-Gaussian operations appearing in generic Clifford circuits violate the total parity $\bar{Z} = \prod_{l=1}^{L} Z_l$. In general, a parity-breaking Pauli operator, e.g., a single X or Y, maps to an odd-length string of Majorana fermions attached to one (without loss of generality, the left) spatial boundary of the circuit. For Clifford circuits, two consecutive parity-violating measurements, say, X_l followed by X_m, are equivalent to one parity-violating measurement (X_m) followed by one parity-conserving measurement ($X_l X_m$). While the latter can be treated by the discussion of Jordan-Wigner strings in the previous section, the former requires additional care. Here, we show that, under appropriate conditions, such a pair of parity-violating measurements may be reduced to a short-range measurement $\mathcal{P}$ followed by a long-range swap $\mathcal{R}$ in the Majorana framework. Depending on the measured operators and, in particular, their spatiotemporal location, such swaps are nonlocal in spacetime and may bridge large distances. Moreover, these swaps yield a potential mechanism for violating orientability, allowing a CPLC Goldstone phase to emerge.

In order to include general parity-breaking measurements in the Majorana framework, we recast them as parity-preserving ones by introducing two ancilla fermions [142]. We place an ancilla qubit A consisting of two Majorana modes γ_{A_1} and γ_{A_2} at the left boundary of the system, as in Fig. 5. Performing a Z_A measurement followed by a Hadamard gate, the ancilla is prepared in an eigenstate $\langle X_A \rangle = 1$ without well-defined parity. For a parity-nonconserving operator $\hat{O}$ acting in the bulk, prepending X_A yields a new operator $\hat{O} \to X_A \hat{O} = \gamma_{A_1} \hat{O}$ that is even in Majorana modes. This now conserves the parity of the joint system $Z_A \bar{Z}$ and leaves the bulk unmodified compared to measuring only $\hat{O}$.

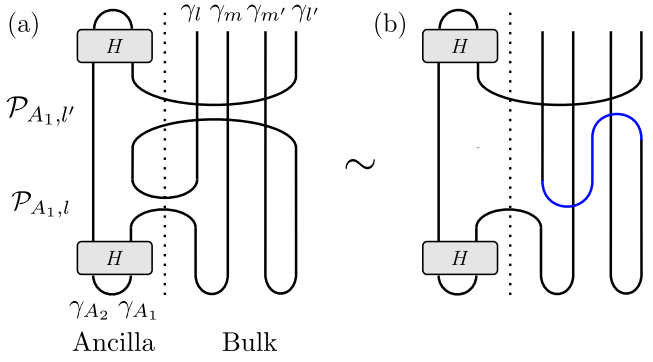

FIG. 5. Ancilla-mediated parity-nonconserving measurements. (a) Two sequential single Majorana measurements mediated via an ancilla qubit $\mathcal{P}_{A_1,l}$ at time t and $\mathcal{P}_{A_1,l'}$ at time t'. At the end of the evolution, the ancilla is decoupled from the bulk by a measurement in the X basis. (b) An equivalent circuit generating the same final state involves a connection (blue) of bulk loops that is nonlocal in both space and time. This can be viewed as an effective swap $\mathcal{R}_{l,l'}$ after the first measurement $\mathcal{P}_{A_1,l}$. If γ_l and $\gamma_{l'}$ are in separate bipartitions of the Majoranas, this effective swap facilitates a breaking of the worldline orientability.

To illustrate the effect of the ancilla, we consider the following basic example, as depicted in Fig. 5. Consecutively measure two single Majorana fermions: $\hat{O} = \gamma_l$ at time t and $\hat{O}' = \gamma_{l'}$ at time t'. In the ancilla framework, this yields the Gaussian projections $\mathcal{P}_{A_1,l} = \frac{1}{2}(1 + i\gamma_{A_1}\gamma_l)$ at time t and $\mathcal{P}_{A_1,l'}$ at time t'. Both can be expressed in the loop model framework by connecting the ancilla worldline $\gamma_{A,1}$ to bulk worldlines $\gamma_l(t)$ and $\gamma_{l'}(t')$. Between times t and t', this is equivalent to drawing a direct loop between $\gamma_l(t)$ and $\gamma_{l'}(t')$, i.e., replacing the ancilla loop by a spacetime nonlocal swap $\mathcal{R}_{(l,t),(l',t')}$. Any two consecutive, single-Majorana measurements γ_{l_n} and $\gamma_{l_{n+1}}$ at times $t_n < t_{n+1}$ can, thus, be replaced by a swap $\mathcal{R}_{(l_n,t_n),(l_{n+1},t_{n+1})}$. By this procedure, the ambiguity in the bulk parity persists only along the loop connecting the first and the final parity-breaking measurement via the ancilla. After the final parity-violating measurement, the ancilla is removed by applying another Hadamard gate and then measuring Z_A. In the bulk, this implements a final swap $\tilde{\mathcal{R}}_{(l_N,t_N),(l_1,t_1)}$, which pushes the parity ambiguity into the qubit represented by the pair $\gamma_{l_1}\gamma_{l_N}$.

When measuring local Pauli operators, e.g., X or ZX, the effects of both the ancilla of JW strings need to be combined. Each measurement then results in a superposition of all possible loop configurations, including long-range swaps, which are compatible with the state in the circuit, e.g., as in Eq. (6). In a short-loop phase, this again yields only a few possibilities so that the main effects of parity-breaking measurements are orientability breaking and long-range swaps. By contrast, in a phase with extended loops, parity-breaking measurements generate superpositions of many worldline configurations, leading to a rapid growth of entanglement.

III. LOOP MODEL PHASES IN MEASUREMENT-ONLY CIRCUITS

We now turn our attention toward a family of measurement-only circuits, based on (next-)nearest-neighbor qubit measurements. We show that such circuits realize phases and phase transitions that are described by Majorana loop models. In each case, our starting point is a local, Gaussian circuit. We distinguish orientable and nonorientable circuits based on bipartiteness of the underlying Majorana graph, which is equivalent to measuring time-reversal symmetric operators. A summary of the setup and the corresponding phase diagrams for orientable and nonorientable circuits are

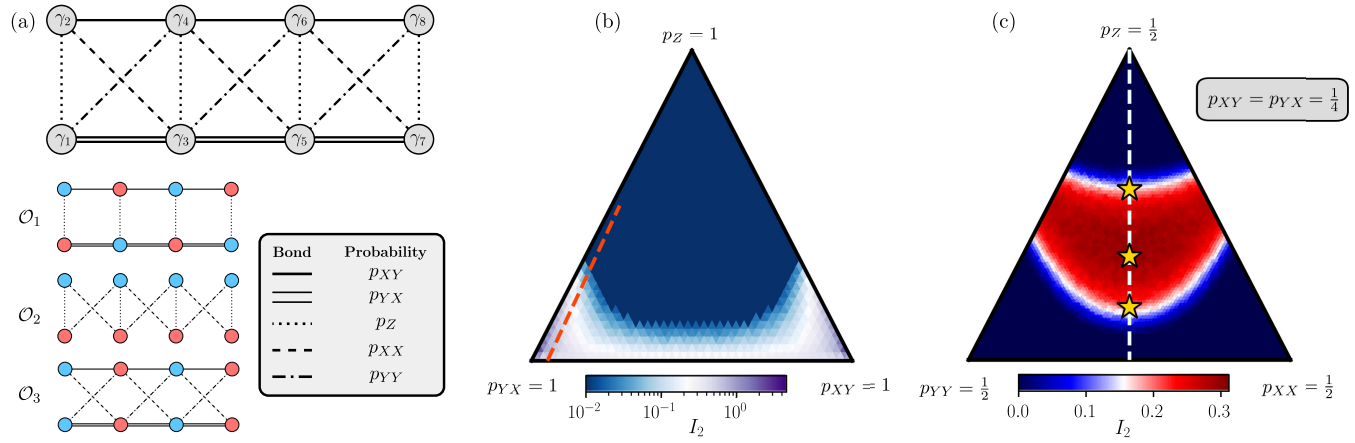

FIG. 6. Loop model for Gaussian Majorana circuits. (a) Each allowed two-fermion parity check is represented by a bond on the lattice. The probability for each bond to be measured and the corresponding Pauli operator are shown in the table. Each orientable set $\mathcal{O}_{1,2,3}$ yields a different bipartition of the lattice. (b) Phase diagram of the $\mathcal{O}_1$ ladder with $p_Z + p_{XY} + p_{YZ} = 1$ for system size $L = 1024$. For $p_Z > 0$, the circuit is in an area-law state, which is highlighted by the rapid vanishing of entanglement on a logarithmic scale. At large anisotropy ($|p_{XY} - p_{YZ}| \approx 1$), rare Z measurements induce a peculiar state with exponentially large correlation length, i.e., a strongly enhanced mutual information, and tunable correlations between the two legs of the ladder. The dashed red line along $q = 0.05$ corresponds to the parameter interval examined in Fig. 7. (c) Phase diagram of a nonorientable circuit in the $p_{XX} + p_{YY} + p_Z = \frac{1}{2}$ plane at fixed $p_{XY} = p_{YX} = \frac{1}{4}$, given by the two-interval mutual information I_2 for system size $L = 4096$. The extended phase with finite I_2 is the Goldstone phase. The white dashed line gives the $p_{XX} = p_{YY}$ cut used in Fig. 9. The marked points give exemplary points which are either on the critical line or deep within the Goldstone phase.

shown in Figs. 6(a)–6(c). When orientable, the Gaussian circuits realize loop models corresponding to variants of the one-state Potts model and critical behavior corresponding to the 2D bond percolation universality class. In contrast, nonorientable Gaussian circuits are described by the CPLC and feature a transition into the symmetry-broken Goldstone phase.

We then add non-Gaussian measurements that may or may not preserve the symmetry (i.e., orientability) of the underlying Gaussian circuit. In the orientable case, we observe the emergence of a family of loop models, which are connected to the TL or Brauer algebra of (coupled) Potts models. Conversely, in the nonorientable case, we find a robust CPLC Goldstone phase: It appears for any type of nonorientable circuit as soon as orientability is broken sufficiently strongly.

Restricting the measured operators to single or nearest-neighbor qubits yields exactly five types of Pauli operators that are Majorana bilinears: $\mathcal{O} = \{Z_l, X_l X_{l+1}, Y_l Y_{l+1}, X_l Y_{l+1}, Y_l X_{l+1}\}$. It is then convenient to represent the corresponding Majorana circuit on a weighted graph; see Fig. 6(a). Each vertex γ_l of the graph corresponds to a Majorana fermion, and each bond $\hat{O} = i\gamma_l\gamma_m$ specifies a parity check, measured with probability p_O. For the set of Paulis $\mathcal{O}$ given above, this graph has the structure of a two-leg ladder, shown in Fig. 6(a). We consider a translationally invariant circuit such that any two identical bonds are measured with the same probability. Each temporal "layer" of the circuit corresponds to a unit time step $\Delta t = 1$ and consists of L independent random measurements. For each measurement, a Majorana $l \in \{1, 2, \ldots, 2L\}$ is selected at random with uniform probability. We then measure an operator $\hat{O} = i\gamma_l\gamma_m$ which is randomly drawn from the probability distribution p_O.

A. Orientable Gaussian circuits

From the set of allowed Pauli operators, one can form three translationally invariant and orientable subsets:

$$\mathcal{O}_1 = \{Z_l, X_l Y_{l+1}, Y_l X_{l+1}\},$$
$$\mathcal{O}_2 = \{Z_l, X_l X_{l+1}, Y_l Y_{l+1}\},$$
$$\mathcal{O}_3 = \{X_l Y_{l+1}, Y_l X_{l+1}, X_l X_{l+1}, Y_l Y_{l+1}\}.$$

The corresponding bipartite Majorana graphs are shown in Fig. 6(a). It is convenient to define two global unitary transformations $U_Z \equiv \exp[i(\pi/4)\sum_l Z_l]$ and $U_{Z,\mathrm{odd}} \equiv \exp[i(\pi/4)\sum_l Z_{2l-1}]$, consisting of a $\pi/2$ rotation of each or each odd Pauli-Z (i.e., a product of the $\mathcal{R}_{2l-1,2l}$ operators). Application of $U_{Z,\mathrm{odd}}$ maps $\mathcal{O}_1 \leftrightarrow \mathcal{O}_2$, making the two circuits identical upon parity sign flips, and it leaves $\mathcal{O}_3$ invariant. Application of U_Z leaves all three subsets invariant.

1. Potts models and percolation

Each orientable subset $\mathcal{O}_{1,2,3}$ contains at least one further subset of operators whose projectors form a TL algebra. For instance, the set of measurements $\{Z_l, X_l X_{l+1}\} = \{i\gamma_{2l-1}\gamma_{2l}, i\gamma_{2l}\gamma_{2l+1}\}$ forms the TL algebra generated by

$\{b_l = \mathcal{P}_{l,l+1}\}$. The evolution of the circuit is then described by the transfer matrix

$$\begin{aligned} T &= T_1 T_3 \ldots T_{L-1} T_2 T_4 \ldots T_L, \\ T_{2l-1} &= 1 + p_Z b_{2l-1}, \\ T_{2l} &= 1 + p_{XX} b_{2l}, \end{aligned} \tag{7}$$

which is identical to the transfer matrix in the 2D one-state Potts model. Depending on the probabilities p_Z and p_{XX}, the odd (b_{2l-1}) or even (b_{2l}) parity measurements dominate. This yields a dimerized ground state in the Potts model given by a configuration of short loops over even or odd bonds. The latter is equivalent to a stationary state in the circuit with dimerized Majorana parities that features area-law entanglement and zero (one) pairs of Majorana edge states for $p_Z > p_{XX}$ ($p_Z < p_{XX}$).

The transition between the two topologically inequivalent area-law states at $p_Z = p_{XX}$ is described by the critical one-state Potts model, corresponding to the universality class for 2D bond percolation. In the loop framework, this yields an algebraic distribution of loop lengths ℓ, $P(\ell) = 3\log(2)\tilde{c}\ell^{-2}$, and logarithmically growing entanglement entropy $S_L \sim (\tilde{c}/3)\log(L)$ with $\tilde{c} = [3\sqrt{3}\log(2)/2\pi]$ [86,126] (see Table I). The universality of this transition has been confirmed in previous works, where measurements of the set $\{Z_l, X_l X_{l+1}\}$ are motivated as a *projective Ising model* [59,143] or a measurement-only version of the *repetition code* [62,110]. Applying $U_{Z,\mathrm{odd}}$, U_Z, or their product to $\{Z_l, X_l X_{l+1}\}$ yields three further sets of measurements that realize the same TL algebra and, thus, the same universal behavior. Since both U_Z and $U_{Z,\mathrm{odd}}$ correspond to constant-depth local unitary circuits, the topology of the two area-law states is preserved—local swaps transform the dimerization pattern but do not add or remove edge modes.

Two further *independent* TL algebras $\{d_l = \mathcal{P}_{2l-1,2l+1}\}$ and $\{f_l = \mathcal{P}_{2l,2l+2}\}$ are realized by the sets $\{Y_l X_{l+1}\} = \{i\gamma_{2l-1}\gamma_{2l+1}\}$ and $\{X_l Y_{l+1}\} = \{i\gamma_{2l}\gamma_{2l+2}\}$. Application of U_Z exchanges $\{d_l\} \leftrightarrow \{f_l\}$, while under $U_{Z,\mathrm{odd}}$, $\{Y_l X_{l+1}\} \leftrightarrow \{X_{2l-1}X_{2l}, Y_{2l}Y_{2l+1}\}$ and $\{X_l Y_{l+1}\} \leftrightarrow \{Y_{2l-1}Y_{2l}, X_{2l}X_{2l+1}\}$. Together, the two sets realize two *independent* one-state Potts models. While, in principle, the parameters for these Potts models can be tuned independently, translational invariance of the measurement probabilities yields an additional constraint. For the set $\{Y_l X_{l+1}, X_l Y_{l+1}\}$, translational invariance places both Potts models exactly at the critical point [144] but with distinct timescales fixed by p_{XY} and p_{YX}. In contrast, for the set $\{X_l X_{l+1}, Y_l Y_{l+1}\}$, both Potts models are identical but can be tuned through different phases.

Once we extend the measurements to include any full subset $\mathcal{O}_{1,2,3}$, the circuit remains orientable but is no longer described by uncoupled TL algebras. Instead, the Potts models are coupled by a relevant, Gaussian operator. Below, we consider one particular case of such coupled Potts models in the Gaussian circuit.

2. Relation to the Ising model ground state

It is instructive to compare the percolation transition in the "projective Ising model" to the ground state phase transition in the Ising Hamiltonian. To do so, we first realize that the Ising Hamiltonian can be expressed in terms of projectors:

$$\begin{aligned} H &= \sum_l J X_l X_{l+1} + h Z_l \\ &= -2\sum_l J\mathcal{P}_{2l,2l+1} + h\mathcal{P}_{2l-1,2l} + K, \end{aligned} \tag{8}$$

where $K \in \mathbb{R}$ is an irrelevant constant. The ground state of the Hamiltonian is obtained from some random initial state $|\psi_0\rangle$ by imaginary time evolution $|GS\rangle = \lim_{\beta\to\infty} e^{-\beta H}|\psi_0\rangle / \sqrt{\langle\psi_0|e^{-2\beta H}|\psi_0\rangle}$. Importantly, and in contrast to the evolution by measurement, here the normalization is performed only at the end of the evolution and not after individual application of the projectors. Trotterizing the time evolution yields $e^{-\beta H} = (1 - \delta_\tau H)^{\beta/\delta_\tau}$ for $\delta_\tau J, \delta_\tau h \ll 1$. Each Trotterized evolution step corresponds to an application of $1 - \delta_\tau H$, i.e., a transfer matrix of the form of Eq. (7) with $p_{XX} = \delta_\tau J$, $p_Z = \delta_\tau h$. However, due to the different normalization, the transfer matrix contains generators of a TL algebra, which results from an exact operator identity and, thus, has loop fugacity $n = \sqrt{2}$. The transfer matrix in this case, thus, describes the $n^2 = 2$-state Potts model, which is the Ising model. The subtle distinction in the algebras underlying imaginary time evolution and measurement, thus, yields two different universality classes. Physically, this effect is very transparent: In the imaginary time evolution, the normalization at the end makes sure that states with different energy are weighted differently, expressed by an increased loop fugacity in the loop model. In contrast, measurements do not provide a notion of energy and, instead, weigh all energetic configurations equally, implemented through loop fugacity $n = 1$.

3. Apparent criticality altered by measurement

Consider the orientable set $\mathcal{O}_1$. It realizes two critical one-state Potts models, represented by the chain of either the even $\{X_l Y_{l+1}\}$ or the odd $\{Y_l X_{l+1}\}$ Majorana modes. The two are coupled by measurements of $\{Z_l\}$. This Gaussian term is relevant and introduces a timescale and length scale, pushing the circuit into an area-law phase. However, when both critical Potts models have significantly different characteristic timescales, i.e., for strong anisotropy between the measurement probabilities, the correlation length remains exponentially large in the inverse interchain coupling strength $1/p_Z$; cf. Fig. 6(b).

This yields an intriguing dynamical regime: A circuit of finite size or depth displays long-range correlations and apparent critical behavior, up to exponentially large distances, which is tunable by $\{Z_l\}$ measurements—a general feature when Potts models are weakly coupled by a relevant operator.

Let us define $q = \min\{p_{YX}, p_{YX}\}/(p_{XY} + p_{YX})$, which measures the anisotropy between the two Potts models. At strong anisotropy and weak coupling, i.e., $q, p_Z \ll 1$, the typical timescale on which each of the two Potts models evolves is $\approx q^{-1}, (1-q)^{-1}$. Weak coupling between the two models then provides an additional channel for the *slow* Potts model to spread correlations via the *fast* one. Consider, for instance, the case $p_{YX} \ll p_{XY}$ such that odd Majoranas $\{\gamma_{2l-1}\}$ evolve much faster than even ones $\{\gamma_{2l}\}$. In order for a pair $\gamma_{2l}\gamma_{2l+2m}$ on the slow chain to become entangled, a loop end point must travel m sites. This can be accomplished either by waiting $\geq q^{-m}$ layers for rare, even-mode measurements or by taking the fast lane, harnessing frequent odd-mode measurements to travel the same distance in $\geq (1-q)^{-m} p_Z^{-2}$ layers. At long distances $m \gtrsim 2\log(p_Z)\log[q/(1-q)]$, the latter process dominates. Correlations in the slow chain are then significantly enhanced by the weak coupling. Hence, the fast (slow) Potts model acts as a bath for the slow (fast) one, enhancing (reducing) its tendency to form long loops $\ell \gg 1$. A similar scenario is observed in other monitored quantum systems, in particular, when coupling two critical Ising chains by measurements [145].

The modification of the length distribution $P(\ell)$ for loops within and between the two Majorana chains is seen in Fig. 7. Both intrachain distributions converge to an approximate power law $\ell^2 P(\ell) \to \alpha_\ell$, whereas α_ℓ decays very slowly with ℓ on a logarithmic scale. This reflects the exponentially large correlation length ξ, such that for loop lengths $\xi > \ell \gg 1$ a power-law behavior, reminiscent of a critical state, is observed. As a consequence, each individual chain displays a logarithmic growth of the entanglement entropy at finite system size. For the slow (fast) chain, the magnitude of the probability density is enhanced (reduced) by roughly one order of magnitude. Long loops are almost exclusively accumulated in the slow chain and, to a lesser extent, between the chains. From the asymptotic value $\lim_{\xi>\ell\gg 1} \ell^2 P(\ell) = (\tilde{c}/3)$, we can extract the coefficient $\tilde{c}$ for the logarithmic growth of the intrachain entanglement entropy $S_{L/2} = (\tilde{c}/3)\log(L)$, shown in Fig. 7(b). This value is no longer universal. Instead, it can be tuned to arbitrary values by adjusting the measurement probabilities p_Z and q and thereby the anisotropy between the Potts models and their coupling strength. Since the correlation length ξ diverges for $p_Z \to 0$, this provides a knob to control both the amount of long-range correlated loops in each individual chain as well as the length scale up to which the apparent critical behavior can be observed.

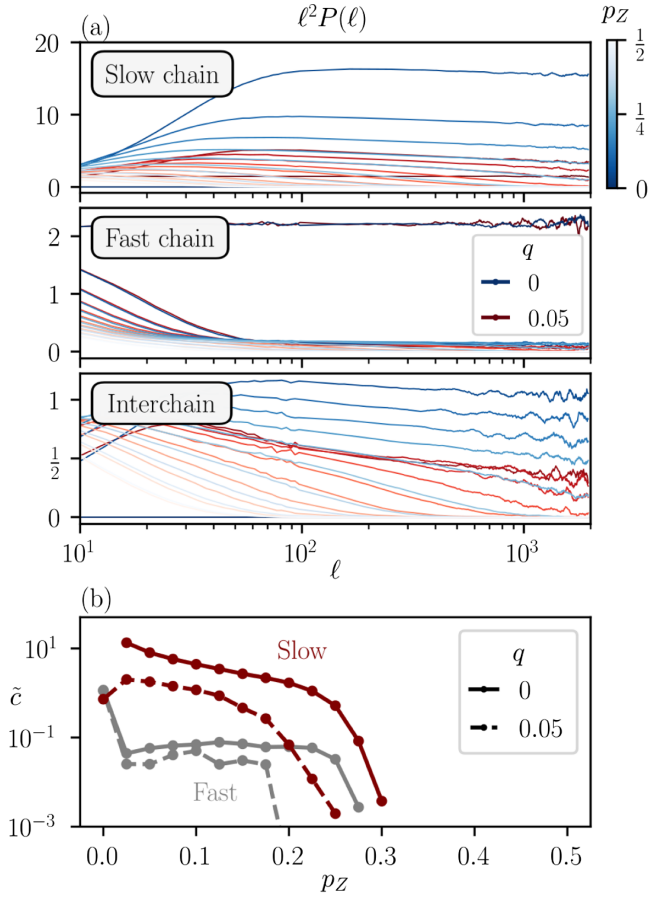

FIG. 7. Measurement-altered criticality for orientable Gaussian circuits: Taking large anisotropy $q = \min\{p_{XY}, p_{YX}\}/(p_{XY} + p_{YX})$, a small but finite interchain coupling via $p_Z \neq 0$ alters the criticality of otherwise decoupled chains. (a) Length distributions for fermionic loops restricted to either chain or spanning between the two chains. The slow and fast chains see a strong enhancement and suppression, respectively, of long-loop probability at finite coupling p_Z. At large ℓ, $\ell^2 P(\ell)$ approaches a constant when $q = 0$ (blue) and decays very slowly at $q = 0.05$ (red) in the slow chain, corresponding to approximately critical entanglement induced via the coupling. For weak coupling, the fast chain also exhibits almost constant $\ell^2 P(\ell)$, indicating that criticality is modified but not destroyed. The interchain loop length distribution shows that finite entanglement is shared between the chains at long distances. (b) The effective log-law coefficient $\tilde{c}$ in each chain extracted from the asymptotic value of $\ell^2 P(\ell)$ at fixed system size L. This reflects the enhanced magnitude of $\tilde{c}$ in the slow chain at weak coupling and the reduced but finite criticality of the fast chain.

We note that similar scenarios have emerged in related, orientable loop models; earlier works on coupled network models for the spin quantum Hall effect show that coupling two critical one-state Potts models via a Gaussian operator immediately opens a gap, leading to a finite but large correlation length [87,146]. Furthermore, the orientable boundary of the CPLC phase diagram studied in Ref. [100] gives rise to a coupled Potts model interpretation, for which

the correlation length grows exponentially large with the tuning parameter.

B. Orientable non-Gaussian circuits

Let us now consider measuring the orientable subset $\mathcal{O}_3 = \{X_l X_{l+1}, Y_l Y_{l+1}, Y_l X_{l+1}, X_l Y_{l+1}\}$ and the non-Gaussian operators $\{Z_l Z_{l+1}, X_l X_{l+2}\}$. The latter are compatible with orientability but introduce eight-leg vertices into the loop diagram. This prohibits a precise microscopic mapping to a TL algebra for the circuit. Nonetheless, we can construct an effective transfer matrix based on the TL algebra of the Gaussian operators, and we show that it accurately describes the dynamics in the circuit. The structure of the transfer matrix is again familiar from the statistical mechanics of coupled Q-state Potts models [106]. We argue that this approach is general for both Gaussian and non-Gaussian orientable circuits and, thus, establishes close contact between one-dimensional measurement-only circuits and 2D Potts models.

Adding symmetry-preserving, non-Gaussian measurements is an irrelevant perturbation to an extended phase of Gaussian measurements, though it may become relevant in the vicinity of a Gaussian critical point. Furthermore, when non-Gaussian measurements become the dominant generator of evolution, they may drive the circuit toward a strong-coupling fixed point. In the following, we discuss three general examples for this scenario: (i) By adding non-Gaussian measurements in the vicinity of the percolation critical point of the one-state Potts model, we split the critical point into two BKT transitions, which enclose an emergent critical phase, (ii) when inducing additional frustration by measuring incommensurate non-Gaussian operators, the critical phase transforms into a volume-law entangled phase, and (iii) when non-Gaussian measurements dominate, they give rise to a strong-coupling tricritical point with an emergent Ising universality. We show how (i)–(iii) can be understood from an elementary version of the problem admitting an exact algebraic description.

We consider a simplified version of the circuit, based on measuring the Gaussian operators $\{XY, YX\}$ with probability $(s/2) \equiv p_{XY} = p_{YX}$ and the non-Gaussian operators $Z_l Z_{l+1}$ and $X_l X_{l+2}$ with probabilities $p_{ZZ} = (1-s)r$ and $p_{XIX} = (1-s)(1-r)$, respectively. The phase diagram in Fig. 8(c) shows the different transitions realizing scenarios (i)–(iii). Here, the choice of Gaussian operators admits a pair of TL algebras with generators $e_l \equiv \mathcal{P}_{2l-1,2l+1} = \frac{1}{2}(\mathbb{1} + X_l Y_{l+1})$ and $f_l \equiv \mathcal{P}_{2l,2l+2} = \frac{1}{2}(\mathbb{1} + Y_l X_{l+1})$, respectively. The transfer matrix for the Gaussian circuit then is equivalent to that of two uncoupled, critical one-state Potts models. Treating the non-Gaussian operators as a perturbation, the transfer matrix T for the interacting circuit

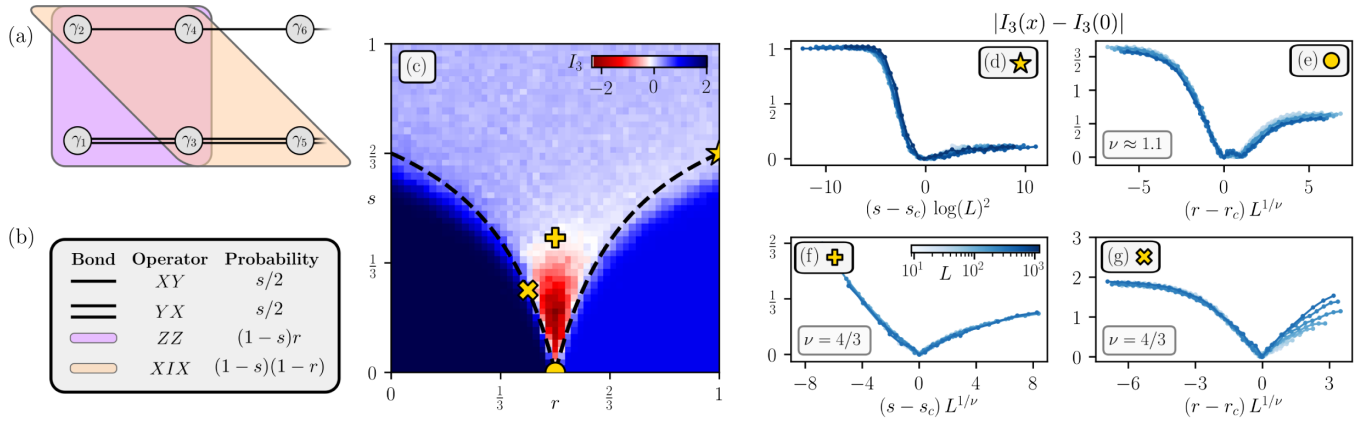

FIG. 8. Orientable non-Gaussian circuit. (a) Majorana lattice for the two-leg ladder with four-fermion measurements. Shaded plaquettes denote $Z_l Z_{l+1}$ (purple) and $X_l X_{l+2}$ (orange) measurements. (b) Probabilities for the allowed two- and four-fermion measurements. Quantity $s \in [0, 1]$ sets the relative probability for two-fermion versus four-fermion measurements, while r determines which type of four-fermion terms are measured. (c) Phase diagram in the $r - s$ plane showing three distinct phases: an area-law phase at strong four-fermion measurement rate, a critical phase extending from the noninteracting limit, and a volume-law phase arising from frustration between four-fermion terms. The dashed black line marks the analytic expression for the critical point $s_c = 2|2r-1|/(1+2|2r-1|)$. The apparent deviation of the data from expected critical line results from finite-size effects which are particularly strong for larger $|r - \frac{1}{2}|$, where the BKT transition gives logarithmically slow convergence to the thermodynamic limit. (d)–(g) Critical rescaling of the tripartite mutual information I_3 along various cuts in the $r - s$ plane. In all plots, the critical value $I_3(x = 0)$ is subtracted off and data are shown for system sizes up to at least $L = 360$. (d) When $r = 1$, the critical and area-law phases are separated by a BKT transition at $s_c = \frac{2}{3}$. (e) With only interactions ($s = 0$), the two area-law phases are separated by a conventional second-order transition at $r_c = \frac{1}{2}$ with critical exponent $\nu \approx 1.1$, close to the expected $\nu = 1$ for Ising criticality. (f) Fixing $r = \frac{1}{2}$, we observe a percolation transition between a critical phase and a volume-law phase with logarithmic corrections. (g) A cut at $s = \frac{1}{4}$ reveals a percolation transition with $\nu = \frac{4}{3}$ separating the area- and volume-law phases.

can be expressed in terms of the original TL generators (see Appendix C):

$$T = \sum_i [\lambda(e_i + f_i) + e_i((1+\delta r)f_i + (1-\delta r)f_{i+1})],$$
$$\lambda \equiv \frac{s}{2(1-s)} - |\delta r|, \qquad \delta r \equiv 2r - 1. \tag{9}$$

We now go through scenarios (i)–(iii) in the phase diagram with the help of the transfer matrix T.

1. Emergent critical phase and splitting of the percolation critical point into two BKT transitions

Consider the limit $s \to 1$ and $\delta r = \pm 1$, which corresponds to two one-state Potts models, which are tuned toward their critical point. Each is described by a TL algebra $\{e_i\}, \{f_i\}$. Then adding measurements of either $\{Z_l Z_{l+1}\}$ or $\{X_l X_{l+2}\}$ introduces the couplings $e_i f_i$ or $e_i f_{i+1}$, which both generate yet another TL algebra for a single, critical one-state Potts model. This coupling is known to be an irrelevant perturbation [106], and, thus, for $\lambda > 0$ the critical Gaussian state remains robust. Increasing the rate of non-Gaussian measurements, the circuit reaches a strong-coupling fixed point at $\lambda = 0$, i.e., at a critical $s = s_c = \frac{2}{3}$. Here, the two critical one-state Potts models combine into a single emergent one. For $\lambda < 0$, i.e., $s < s_c$, non-Gaussian measurements dominate and induce an area-law phase, whose topological properties depends on the sign of δr. With $\delta r = 1$ the area-law phase is trivial, whereas for $\delta r = -1$ one pair of edge states $\sim i\gamma_1\gamma_{2L}$ is stabilized; see Fig. 8(a). In both cases, the phase transition in the coupled Potts models follows a BKT scenario, which is visualized by the finite-size scaling collapse of the mutual information in Fig. 8(d).

When moving away from the limit $\delta r = \pm 1$, both $e_i f_i$ and $e_i f_{i+1}$ appear simultaneously, reflecting the competition between the two types of non-Gaussian measurements. For any δr, the dominant non-Gaussian term induces a robust area-law phase for $\lambda < 0$, which becomes unstable for $\lambda \geq 0$. This yields a precise analytical estimate for the phase boundary at $s = s_c(\delta r) = (2|\delta r|/1 + 2|\delta r|)$, which is confirmed in Fig. 8(c). For large anisotropy δr between the two couplings $e_i f_i, e_i f_{i+1}$ or for large $\lambda > 0$, the Gaussian critical phase remains robust. This is accompanied by a BKT transition into the area-law phase at critical s_c. Numerical simulations of the circuit witness an extended critical phase for $\frac{1}{3} \lesssim s$ and correspondingly a BKT transition for $\frac{1}{4} \lesssim |\delta r|$.

The emergence of a robust critical phase, separated by a BKT critical line from an area-law regime, appears to be generic when symmetry-preserving non-Gaussian measurements are added to the sets $\mathcal{O}_{1,2,3}$. The prerequisite is that the unperturbed circuit is in the vicinity of the one-state Potts model critical point. We show in Appendix D that non-Gaussian measurements cause the single one-state Potts model critical point to branch out into two separate BKT transitions, which enclose an extended critical phase. This might be understood as follows. When an orientable set $\mathcal{O}_{1,2,3}$ is pushed to a percolation critical point, it can be decomposed into two one-state Potts models, one of which is critical. Non-Gaussian measurements then couple both Potts models into a robust critical phase. The scenario in Fig. 8 represents one side of the broadened transition between two area-law phases. A similar picture is observed for orientable Gaussian measurements, which at the critical point are perturbed by unitary gates [147].

2. Tricritical strong-coupling fixed point: Emergent Ising universality

The two critical lines with $\lambda = 0$ meet at the critical point $(s, \delta r) = (0, 0)$; see Fig. 8(c). The merging of two critical lines is typical for a fine-tuned tricritical point, which then realizes a different universality class. Indeed, it is shown that the tricritical point of the ferromagnetic Q-state Potts model with $\sqrt{Q} = 2\cos(\pi/k)$ is related to the critical point of the ferromagnetic Q'-state Potts model, with $\sqrt{Q'} = 2\cos[\pi/(k+1)]$, via the so-called $\epsilon - \eta$ duality [72,148–151]. We argue above that each critical line at $\lambda = 0, \delta r \neq 0$ corresponds to a single, critical one-state Potts model, i.e., $k = 3$. The duality then predicts the tricritical point at $(s, \delta r) = (0, 0)$ to be described by a critical two-state Potts model ($k = 4$), i.e., the Ising universality class. This can be made rigorous by recalling that, in the Potts model, four-spin interactions (e.g., the $e_i f_i$ coupling terms) are mapped to vacancies under a duality transformation [69,152–154]. This maps the two coupled, dense Potts models to a single, dilute one-state Potts model in which s tunes the temperature and δr tunes the vacancy density away from the critical point. Tuning $(s, \delta r) \to (0, 0)$ takes the model to its tricritical point, and the $\epsilon - \eta$ duality yields the critical Ising model.

Numerical simulations confirm the correlation length critical exponent $\nu \approx 1$ of the Ising universality class [see Fig. 8(c)]. In order to further support the emergent Ising universality, we extract the bulk and surface critical behavior through coupling the circuit to ancilla (see Appendix F). This provides information on out-of-time ordered correlation functions and yields the critical exponents $\eta \approx 0.24$ in the bulk and $\eta_\parallel \approx 1.1$ at the surface. Both are compatible with the Ising values $\eta = 1/4$ and $\eta_\parallel = 1$ [155]. Furthermore, $\eta_\parallel = 1$ is consistent with the scaling of the mutual information, which is obtained in Ref. [156] for ZIZ and XX measurements.

We note three peculiar points: (i) Replacing the set $\{X_l X_{l+2}, Z_l Z_{l+1}\}$ by $\{X_l Z_{l+1} X_{l+2}, Z_l Z_{l+1}\}$ yields an identical measurement-frustration graph yet provides a more intuitive picture of the tricritical one-state Potts model. The Gaussian set $\{X_l Z_{l+1} X_{l+2}\}$ realizes two identical Majorana

chains, which are both coupled by $\{Z_l Z_{l+1}\}$ measurements and simultaneously pushed to the critical point. (ii) The same frustration graph is provided by the set $\{X_l X_{l+2} X_{l+3} X_{l+4}, Z_l\}$, which is the measurement-only version of an Ising chain with multispin interactions. The corresponding Hamiltonian has an eightfold-degenerate ground state and is related to the eight-state Potts model [157–165], which undergoes a first-order phase transition. This highlights the observed trend: Orientable measurement-only circuits realize Q-state Potts models, for which Q is reduced compared to their Hamiltonian counterparts. (iii) Despite the critical exponents determining the Ising universality class, we observe an intriguing behavior of the entanglement entropy at the critical point. It grows logarithmically $S_{L/2} = (\tilde{c}/3)\log(L)$ with prefactor $\tilde{c} = 2$. This is significantly larger than the expected value $\tilde{c}_{Q=2} = (1+\sqrt{2})\log(2)/\pi \approx 0.53$ from the loop distribution of the two-state Potts model [126] (see Table I and Appendix F). This discrepancy may result from a difference in boundary conformal field theories between the critical Ising model and the tricritical one-state Potts model.

3. Emerging volume law from competing non-Gaussian measurements

For small anisotropy $|\delta r| \ll 1$ and positive $\lambda > 0$, all the terms in the transfer matrix in Eq. (9) become relevant and none can be treated as a small perturbation. In this regime, the critical phase of the two one-state Potts models for $\lambda > 0$ becomes unstable and the circuit enters a volume-law entangled state. The volume law is signaled by a negative value of the tripartite information I_3 which scales with system size [34,166], shown in Fig. 8(c). The volume-law phase is symmetric around $\delta r = 0$. It is separated from the critical phase of the Gaussian circuit by a critical line at $\tilde{s}_c(r) \approx \frac{1}{3}$ and from the area-law phases by the already-established critical line $\lambda = 0$. At $(s, \delta r) = (0, 0)$, it terminates at the tricritical point. As a consequence, two additional tricritical points emerge at $(s, \delta r) \approx (\frac{1}{3}, \pm\frac{1}{4})$ where all three types of entanglement phases (area law, volume law, and critical) meet. These latter tricritical points are, however, difficult to locate precisely. Along each boundary of the volume-law phase, except for the tricritical points, we find the critical scaling behavior of the one-state Potts model, i.e., percolation; see Figs. 8(f) and 8(g).

While a percolation transition separating a volume-law phase from an area-law phase has been observed previously in measurement-only [58] and monitored unitary circuits [26,104], a percolation transition separating the volume-law and critical phases is unconventional. We observe that the logarithmic growth of the entanglement entropy at this transition remains largely unaltered, while a volume-law contribution emerges on top. A possible explanation of this scenario and of the scaling behavior at the transition might be that the critical sector is decoupled from an otherwise area-law to volume-law transition.

The emergence of the volume-law entangled phase can be explained from two complementary views in the Potts model framework. When starting from the BMW algebra for strongly coupled Potts models, the operator $e_i + f_i$ acts as a perturbation that generates line crossings [106], i.e., emergent swap operations $\mathcal{R}_{\text{eff}}$. For $|\lambda/\delta r| \sim 1$ and $\lambda > 0$, this yields an effective circuit implementing frequent swap operations, which rapidly generate long, orientable loops and, thus, extensive entanglement. For $\lambda < 0$, the same types of swaps arise, but the negative sign results in the cancellation of many trajectories in the partition function, suppressing the mobility of the worldlines.

In turn, when starting from the tricritical point at $(s, \delta r) = (0, 0)$, both $\delta r \neq 0$ and $s > 0$ correspond to relevant perturbations, as explained above [69]. The imbalance parameter $\delta r \neq 0$ tunes the chemical potential for vacancies in the dual dilute model and drives the system toward an ordered area-law fixed point. Tuning $s > 0$ reintroduces the generators e_i and f_i of the original one-state Potts models. In the dual framework, taking finite s corresponds to tuning the temperature and pushing the two-state Potts model into its high-temperature phase. This removes the energetic penalty for forming long loops in the bulk and yields a disordered, volume-law entangled state at the temporal boundary of the circuit.

C. Nonorientable Gaussian circuits

Once the set of measured Gaussian operators no longer admits a bipartition of the Majorana graph, e.g., the union of $\mathcal{O}_{1,2,3}$, the circuit is no longer orientable. The evolution then maps to a loop model which is described by the Brauer algebra of CPLC instead of a TL or walled Brauer algebra. For sufficiently strong competition between incompatible measurements, this nonorientable loop model is known to enter an extended long-loop phase, the Goldstone phase. Both the critical point at the boundary of the Goldstone phase as well as the phase itself display universal scaling behavior, which is described by an $\mathbb{RP}^{n-1}$ NLσM [100]. Circuits realizing this Goldstone phase display a peculiar and universal logarithmic correction to entanglement, purification, and bulk correlation functions [100,113,167].

We confirm that nonorientable Gaussian circuits indeed display the universal behavior of CPLC by examining bulk and boundary correlation functions for the following setup. We measure the operators $\{XY, YX\}$ with equal probability $p_{XY} = p_{YX} = \frac{1}{4}$ and add measurements of $\{Z, XX, YY\}$ such that $p_Z + p_{XX} + p_{YY} = \frac{1}{2}$. The circuit is symmetric for $p_{XX} \leftrightarrow p_{YY}$, i.e., under the global unitary U_Z. The two limits $p_Z = 0, \frac{1}{2}$ are both orientable and correspond to two topologically distinct area-law phases. As shown in Fig. 6(c), they are separated by an extended phase with an increased mutual information and entanglement.

By examining a cut along the symmetric point $p_{XX} = p_{YY} = \frac{1}{4}(1-2p_Z) \equiv p$ [white dashed line in Fig. 6(c)], we show that the entangled phase exhibits all key characteristics of the CPLC Goldstone phase.

1. Correlation length critical exponent

Two critical points, $p_{c,1} = 0.12$ and $p_{c,2} = 0.21$, separate the Goldstone phase from the area-law phases. At both points, a finite-size scaling collapse of the mutual information I_2 [Fig. 9(a) [confirms the CPLC exponent $\nu = 2.75$ [100].

2. Loop length distribution

Both critical points feature a power-law scaling of the loop length distribution $P(\ell)$. It approaches a constant $\ell^2 P(\ell) \to \alpha$ with $\alpha \approx 0.64$ in Fig. 9(b), which is consistent with the value from CPLC: $\alpha = (2.035/\pi) \approx 0.648$ arising from the renormalized spin stiffness [32,100]. In the Goldstone phase, the distribution acquires the characteristic logarithmic correction $\ell^2 P(\ell) \sim \beta \log(\ell)$, with $\beta \approx 0.0565$ being consistent with the CPLC value $(1/2\pi^2) \approx 0.0507$ [32,100]; see Table I.

3. Entanglement entropy

We compute the steady-state entanglement entropy $S_A(L)$ of a contiguous subsystem of $|A|$ qubits in a system of size L. For both the critical points and the entangled phase, we make the ansatz $S_A(L) = [\tilde{c}(L)/3]\log_2 \times [(L/\pi)\sin(\pi|A|/L)] + \beta$. The critical points $p_{c,1/2}$ display an expected logarithmic scaling $\tilde{c}(L), I_2(L) \sim \text{const}$, shown in Fig. 9(c). In the Goldstone phase, the logarithmic correction to the loop distribution leads to an enhanced entanglement with $\tilde{c}, I_2 \propto \log(L)$.

The precise form of the entanglement and mutual information follow from the loop length distribution $P(\ell)$. Both can be computed through an appropriate integral over $P(\ell)$ in the continuum limit of the lattice (see Appendix A for details). At the critical points, $P(\ell) = \alpha \ell^{-2}$ yields $I_2 = \alpha \log(4/3)$ and $S_A = \alpha \log(|A|) + \text{const}$. In contrast, the distribution $P(\ell) = \beta \log(\ell/\ell_0)\ell^{-2}$ for cutoff length scale ℓ_0 yields $I_2 = \beta \log(4/3)\log(|A|/\ell_0) + \text{const}$ (we take $|A| = L/8$) and $S_A = \frac{1}{2}\beta[\log(|A|]^2 + \beta \log(|A|)(1 - \log(\ell_0)) + \text{const}$. For universal prefactor $\beta = (1/2\pi^2)$ from CPLC, we expect $I_2 \sim [\log(4/3)/2\pi^2] \log(L) \approx 0.0146 \log(L)$ and $\tilde{c} \sim [3\log(2)/2\pi^2]\log(L) \approx 0.105 \log(L)$. Indeed, the data at $p = \frac{1}{6}$ exhibit a logarithmic growth of I_2 ($\tilde{c}$) with prefactor 0.0194 (0.0974), both comparable to the universal CPLC values.

4. Dynamical purification

A further signature of the Goldstone phase is logarithmic corrections in the mutual information between the two temporal boundaries, i.e., in the spanning number n_s [100].

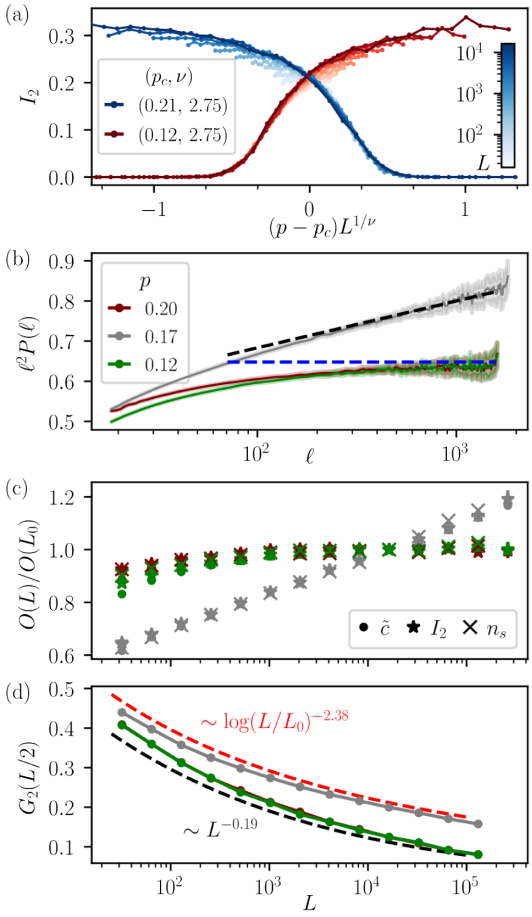

FIG. 9. Nonorientable Gaussian circuit. Data are taken along the line cut in Fig. 6(c) with $p_{XY} = p_{YX} = \frac{1}{4}$ and $p \equiv p_{XX} = p_{YY} = \frac{1}{4}(1-2p_Z)$ in the steady state $T = 8L$ for system sizes up to $L = 2^{17}$. (a) Scaling collapse of the mutual information I_2 identifies the critical points $p_{c,1} = 0.12$ and $p_{c,2} = 0.21$ and a joint critical exponent $\nu \approx 2.75$. (b) Loop length distribution $P(\ell)$ normalized by ℓ^2 to highlight the asymptotic behavior. In the Goldstone phase (gray), CPLC predicts a logarithmic correction $\ell^2 P(\ell) = (1/2\pi^2)\log(\ell)$ (dashed black line). By contrast, at the critical points $p = p_{c,1/2}$ (maroon and green), CPLC predicts a conventional critical scaling $\ell^2 P(\ell) \approx 2.035/\pi$ [100] (dashed blue line). (c) System-size dependence of the log-law coefficient $\tilde{c}$ (circles), mutual information I_2 (stars), and spanning number n_s at circuit depth $T = L$ (crosses), normalized against the value at $L_0 = 2^{14}$. In the Goldstone phase (gray), we observe logarithmic corrections, $O(L) \propto \log(L)$, whereas at the transition $p = p_{c,1/2}$ all three quantities approach a system-size-independent value. (d) The scaling of the two-leg watermelon correlator $G_2(L/2)$ is consistent with CPLC [100]. At the transition, there is power-law decay $G_2(L/2) \sim L^{-2x_2}$ with $x_2 \approx 0.096$ (dashed black line), whereas in the Goldstone phase, correlations decay slower than algebraic, $G_2(L/2) \sim \log(L/L_0)^{-\alpha_2}$ with $\alpha_2 \approx 2.38 \pm 0.2$.

At a conventional critical point with dynamical critical exponent $z = 1$ and for fixed circuit aspect ratio $T = L$, n_s is independent of L. This is confirmed at the critical points $p_{c,1/2}$ and shown in Fig. 9(c). In the Goldstone phase,

however, a logarithmic correction $n_s \propto \log(L)$ appears. This yields logarithmic corrections to the dynamical purification in the circuit when starting from a mixed initial state [113,167]. As a result, there is an anomalous slowing of the purification, which is shown in Appendix B. We find a prefactor of the logarithmic correction of 0.19, whereas $(1/2\pi) \approx 0.159$ is expected from the renormalized spin stiffness in CPLC [100].

5. Bulk correlations

Finally, we examine correlations in the spacetime bulk of the circuit, which are expressed via the two-leg watermelon correlator $G_2(L/2)$. At the critical points $p_{c,1/2}$ in the circuit, $G_2(L/2)$ shows slow power-law decay as L^{-2x_2} with exponent $x_2 = 0.095$ consistent with the behavior in loop models with crossings [100]; see Fig. 9(d). In the Goldstone phase, these correlations fall off even slower, decaying as $G_2(L/2) \propto \log(L/L_0)^{-\alpha_2}$ with a fitted exponent $\alpha_2 = 2.38 \pm 0.2$. Previous work found $\alpha_2 \approx 1.9$ [100], and the slow decay limits the accuracy of the estimate.

D. Nonorientable non-Gaussian circuits

Here, we examine the generality of the CPLC Goldstone phase in nonorientable quantum circuits by adding non-Gaussian measurements. We consider two cases: (i) adding orientable non-Gaussian measurements to a nonorientable Gaussian circuit and (ii) adding nonorientable non-Gaussian, e.g., parity-breaking, measurements to an orientable Gaussian circuit. Orientability is then broken only by the non-Gaussian terms. Both cases yield an extended Goldstone phase with a universal log correction to the entanglement entropy. Since the loop model in the non-Gaussian circuits emerges only on a coarse-grained scale, our main observables are multipartite mutual information measures for Clifford circuits, i.e., the bipartite and tripartite mutual information I_2 and I_3, respectively.

1. Perturbing a CPLC with non-Gaussian measurements

In order to confirm the expected irrelevance of non-Gaussian measurements in both the Goldstone and the area-law phases (see Sec. II E), we examine measurements of the set $\mathcal{O}_3 \cup \{Z_l, Z_l Z_{l+1}\}$. This adds ZZ measurements to the nonorientable setting in Sec. III C. Note that $\mathcal{O}_3 \cup \{Z_l Z_{l+1}\}$ would be an orientable circuit. We set the measurement probabilities to $p_{ZZ} = (1-s)$, $p_Z = p_{XX} = p_{YY} = s(1-p)/3$, and $p_{XY} = p_{YX} = sp/2$, such that the circuit is described by parameters $p, s \in [0,1]$. The Gaussian limit $(s = 1)$ is in a Goldstone phase for $0.22 \lesssim p < 1$. For $s < 1$, the Goldstone phase remains robust against ZZ measurements. Eventually, non-Gaussian measurements become sufficiently frequent to drive the system into an area-law phase. A scaling collapse of the mutual information at the transition confirms the correlation length exponent $\nu \approx 2.75$ as in CPLC [see Fig. 10(e)]. Though they may stabilize an area-law phase at strong

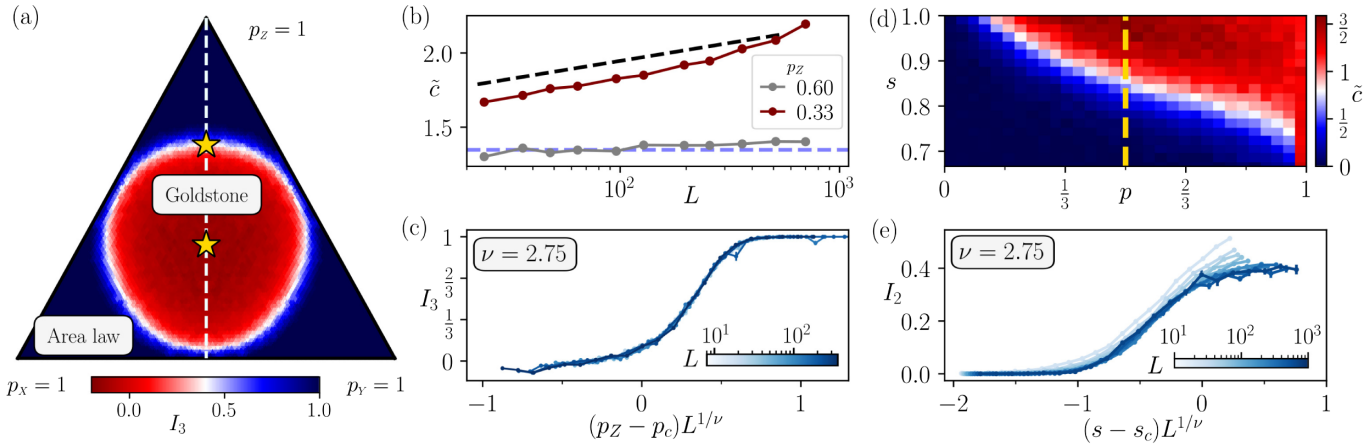

FIG. 10. Measurement phases in non-Gaussian, nonorientable circuits. (a)–(c) Goldstone phase in the range-2 measurement-only circuit where Pauli operators $A_l B_{l+1}$ are measured with probability $p_A p_B$ with $A, B \in \{X, Y, Z\}$. (a) Phase diagram of the tripartite mutual information I_3 showing a Goldstone phase (red) and area-law phase (blue). The white dashed line marks $p_X = p_Y$, along which we mark the upper critical point and the center of the Goldstone phase. (b) The prefactor $\tilde{c}$ of the logarithmic growth of the entanglement entropy. In the Goldstone phase (maroon), we observe a logarithmic correction with magnitude comparable to the universal $3\log(2)/(2\pi^2)$ expected for the CPLC Goldstone phase (black dashed line). At the transition (gray), $\tilde{c}$ is independent of system size and consistent with $\tilde{c} \approx 1.33$ found along the critical line in CPLC. (c) The finite-size scaling collapse of the tripartite mutual information I_3 confirms a critical exponent $\nu \approx 2.75$. (d),(e) Goldstone phase in the interacting, nonorientable two-leg ladder with $p_{ZZ} = 1 - s$, $p_Z = p_{XX} = p_{YY} = s(1-p)/3$, and $p_{XY} = p_{YX} = sp/2$. (d) Phase diagram in the $s - p$ plane showing a transition from a Goldstone phase at weak interactions to an area law where four-fermion measurements dominate. (e) Scaling collapse of the mutual information I_2 along the dashed line in (d) marking $p = \frac{1}{2}$. The scaling is consistent with a critical correlation length exponent $\nu \approx 2.75$, as expected from the Gaussian CPLC limit.

coupling, the non-Gaussian measurements are irrelevant at the CPLC fixed points, leaving the CPLC universality class unaltered.

2. Inducing CPLC by non-Gaussian measurements

Here, we examine the emergence of CPLC, including the Goldstone phase, when adding nonorientable, non-Gaussian measurements to an orientable Gaussian circuit. In particular, we consider Pauli measurements of two qubit operators $A_l B_{l+1}$ with $A, B \in \{X, Y, Z\}$, which form a range-2 measurement-only Clifford circuit [168]. The emergent CPLC in this model further confirms that short-ranged measurement-only Clifford circuits yield emergent loop model behavior, even when including non-Gaussian, parity-violating measurements. Each operator is measured with probability $p_{AB} = p_a p_b$, i.e., $p_{XY} = p_x p_y$, with $p_x + p_y + p_z = 1$. A global rotation $U_A \equiv \exp[i(\pi/4)\sum_l A_l]$ with $A \in \{X, Y, Z\}$ maps between parameters $p_x \overset{U_Z}{\longleftrightarrow} p_y \overset{U_X}{\longleftrightarrow} p_z \overset{U_Y}{\longleftrightarrow} p_x$, yielding a highly symmetric circuit and phase diagram, which is shown in Fig. 10(a).

By virtue of the symmetry above, we can focus on the parameter regime $p_x, p_y \gg p_z$, which corresponds to perturbing the orientable Gaussian circuit $\mathcal{O}_3 = \{XX, YY, XY, YX\}$ with parity-breaking non-Gaussian operators $\{XZ, YZ, ZX, ZY\}$. The parity-breaking operators also break the orientability of the worldlines, as discussed in Sec. II F. Along the orientable boundary $p_z = 0$, we recover the bipartite two-leg ladder, which lies in an area-law phase for all $p_x + p_y = 1$. As in conventional CPLC, the short-loop area-law phase is robust against a small probability of orientability (parity) -violating measurements. Then, at small but nonzero $p_z^{(c)} \approx 0.04$, there is a transition into a CPLC Goldstone phase. The Goldstone phase extends over a large fraction of the parameter range and generally appears when orientability breaking by parity-violating measurements becomes sufficiently strong. The characteristic $[\log(L)]^2$ growth of the entanglement entropy is shown in Fig. 10(b). The critical line separating the Goldstone from the area-law phase features the correlation length exponent $\nu = 2.75$ expected of the CPLC universality class, confirmed in Fig. 10(c).

We note that taking the above example and replacing ZX, XZ, ZY, and YZ measurements by either X or Y measurements alone induces *neither* a nonorientable circuit *nor* a Goldstone phase. The effective swaps emerging from X or Y measurements preserve orientability when added to the set $\mathcal{O}_3$, since products of subsequent measurements, e.g., $X_l X_{l'}$, are obtained from a sequence of measurements from $\mathcal{O}_3$. The same applies to four-qubit operators acting on four consecutive qubits, e.g., $XZXZ$ and $ZXXZ$. The simplest nontrivial, orientability-breaking terms arising from the random two-qubit measurements are the non-Gaussian operators $Z_l X_{l+1} Y_{l+2} \sim Z_l Y_{l+1} \times Z_{l+1} Y_{l+2}$. We demonstrate in Appendix G that including the latter instead of parity-breaking operators indeed yields a CPLC Goldstone phase.

IV. SPACETIME DUALITY

Each $(1+1)$-dimensional quantum circuit possesses a spacetime dual circuit, in which the measurement and swap vertices $\mathcal{P}$ and $\mathcal{R}$ are rotated around $\pi/2$ in spacetime, i.e., for which space and time are exchanged. The loop model of the spacetime dual circuit displays the same bulk behavior, while its spatial boundary correlations, such as the mutual information, are exchanged with the temporal boundary correlations $\sim|\langle\gamma_1(t_2)\gamma_1(t_2)\rangle|$. Depending on the particular loop model, it may be advantageous to implement the spacetime dual instead of the original circuit, e.g., in order to overcome the postselection problem in non-Clifford circuits [11,169–171]. Alternatively, one may implement "isotropic" or spacetime self-dual circuits for which the spacetime dual and the original circuit are identical. This yields an additional symmetry, which may grant access to an exact analytical solution of the circuit evolution [172–182].

Consider, for instance, a circuit with nearest-neighbor Majorana operations, involving only four-leg Majorana vertices. Then the spacetime rotation (i) maps each swap $\mathcal{R}_{l,l+1} \to \mathcal{R}_{l,l+1}$ onto itself (i.e., swaps are self-dual) and (ii) exchanges the identity and the projection $\mathbb{1}_{l,l+1} \leftrightarrow \mathcal{P}_{l,l+1}$. Therefore, the circuit is spacetime self-dual when both $\mathbb{1}$ and $\mathcal{P}$ appear with equal probability.

Allowing nearest-neighbor qubit operations composed of four Majorana fermions requires eight-leg Majorana vertices in spacetime. Let us consider a brick-wall circuit consisting of alternating layers of bricks acting on four neighboring fermions, as depicted in Fig. 11(a). Each brick is an eight-leg vertex in the loop model, with four incoming and four outgoing worldlines, and the set of possible bricks consists of all ways to pair the eight worldlines with one another. Under spacetime rotation, eight-leg vertices transform into one another by permuting the legs [e.g., $1 \to 2', 2 \to 1', 3 \to 1, \ldots$ in Fig. 11(a)]. Among all eight-leg vertices with unambiguous worldline representation, only five are self-dual; see Fig. 11(b).

Let us denote $\mathcal{V}_8$ as the set of all possible configurations of worldline pairings in an eight-leg vertex. The spacetime rotation induces a permutation σ on $\mathcal{V}_8$ such that any vertex $v \in \mathcal{V}_8$ is transformed into $\sigma(v) \in \mathcal{V}_8$. Self-dual vertices have $\sigma(v) = v$, while vertices v_1 invariant under a π rotation but not under a $\pi/2$ rotation have a dual vertex v_2 such that $v_1 \overset{\sigma}{\leftrightarrow} v_2$. The remaining vertices can then be separated into groups of four such that $v_1 \overset{\sigma}{\to} v_2 \overset{\sigma}{\to} v_3 \overset{\sigma}{\to} v_4 \overset{\sigma}{\to} v_1$, since $\sigma^4 = \mathbb{1}$. In a spacetime self-dual circuit, every vertex v and its dual $\sigma(v)$ occur with the same probability P, i.e., $P[\sigma(v)] = P(v)$ for all $v \in \mathcal{V}_8$. This gives rise to an abundance of Majorana brick-wall circuits, which feature both spacetime duality and an exact worldline description.

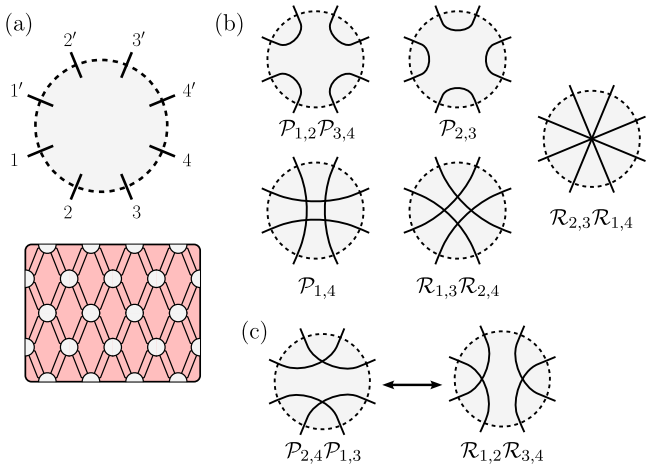

FIG. 11. Spacetime duality in a brickwork circuit. (a) Alternating layers of two-qubit operations give a tilted square lattice where each edge carries two worldlines. Each "brick" in the circuit consists of a generic eight-leg vertex in which the four incoming (unprimed) and outgoing (primed) worldlines must be paired among one another. Exchanging space and time gives a $\pi/2$ rotation of such an eight-leg vertex configuration. (b) The five eight-leg vertex configurations which are self-dual under the spacetime rotation, along with the corresponding operation. If, instead, a $\pi/4$ rotation is made, then two pairs rotate into one another while the four-line crossing $\mathcal{R}_{2,3}\mathcal{R}_{1,4}$ is left invariant. (c) A pair of vertex configurations which transform into one another under the spacetime rotation. For this example, parity checks are transformed into swaps, giving an intuitive picture for how measurements act to mediate effective swaps.

A peculiar scenario arises when v and $\sigma(v)$ correspond to different types of operations, i.e., when v results from a nonunitary operation while $\sigma(v)$ is unitary. This gives rise to the possibility to implement an entirely unitary circuit, which realizes the spacetime dual of a nonunitary circuit including measurements. This approach is demonstrated for Clifford circuits in order to overcome the postprocessing [15] or postselection [183] problem of nondeterministic measurements [11,170].

In the loop model framework, a large class of both orientable and nonorientable circuits can be simulated by purely unitary evolution. However, since the spacetime dual of the identity is a projective parity measurement, only "dense" nonunitary circuits, where each brick realizes either a swap or a measurement but never the identity, have a unitary spacetime dual. This poses a restriction on the corresponding loop model. For instance, the CPLC realized by purely unitary operations lives at the border of the CPLC phase diagram [100] and cannot stabilize a Goldstone phase. Instead, it realizes a gapped area-law phase in both the temporal and the spatial direction, with a parametrically large correlation length. This can be rationalized by the fact that in 2D a bulk phase which breaks a continuous symmetry is allowed only under a nonunitary evolution.

Phase transitions which continuously break a discrete symmetry do not have this constraint in two dimensions. This grants access to the physics of coupled Potts models, e.g., to the Ising and percolation phase transitions, that are observed in orientable circuits also via a purely unitary evolution.

V. LOOP MODELS IN DIFFERENT GEOMETRIES

We now turn our attention to Gaussian measurement-only circuits for which we lift the constraint that measurements be limited to nearest- and next-nearest neighbors. This allows us to manipulate the geometry of the underlying Majorana lattice in order to probe the presence or absence of a Goldstone phase as a function of the circuit's orientability. The starting point here is measurements of the operators Z, XY, and YX and the $XZZX$ stabilizer. This relates the setup to an important class of quantum error correcting codes [184] and to topological phase transitions: For suitable measurement rates, the circuit hosts both a symmetry-protected topological order and a bulk symmetry-breaking order [130,185].

In the presence of $XZZX$-stabilizer measurements, it is convenient to arrange the Majorana fermions on a three-leg ladder geometry as shown in Fig. 12(a). The Z and $XZZX$ measurements implement three copies of the repetition code [130] or, alternatively, a measurement-only version of the fermionic 3-chain obtained by interleaving three Kitaev chains [186]. The chains are coupled via XY and YX Pauli measurements connecting γ_l and γ_{l+2}. This implements vertical bonds between chains $1 \leftrightarrow 2$ and $2 \leftrightarrow 3$, while it creates a relative offset at the boundary, coupling mode n on chain 3 and mode $n+\delta$ with $\delta = 2$ on chain 1. This link, i.e., the offset $\delta = 2$, makes the circuit nonbipartite and its loop model nonorientable. Conversely, an offset $\delta = 1$ instead of $\delta = 2$ would make the graph bipartite and restore orientability.

This argument can be extended to generic m-leg ladders with rectangular interchain bonds between chains $k = 1, \ldots m-1$. Making such a graph bipartite requires Néel ordering of the worldline orientations. This is compatible only with an offset δ between the mth and the first chain if $\delta + m$ is even. Otherwise, the ladder is *not* bipartite, and orientability is broken.

We numerically confirm the presence (absence) of a Goldstone phase for nonorientable (orientable) ladder geometries in Fig. 12(b). It shows the entanglement in the circuit for different offsets δ and measurement probabilities. The latter are parametrized by $p, q \in [0,1]$ as shown in Fig. 12(a). Here, $\frac{1}{2}(1-p)$ is the probability for measuring one of the two interchain bonds, and q sets the dimerization of measurement probabilities along each chain; i.e., $p = 1, q = \frac{1}{2}$ is the percolation critical point of the $XZZX$ code [130]. When δ is odd, only the lines $q = \frac{1}{2}$ and $p = 0$ show increased mutual information, with

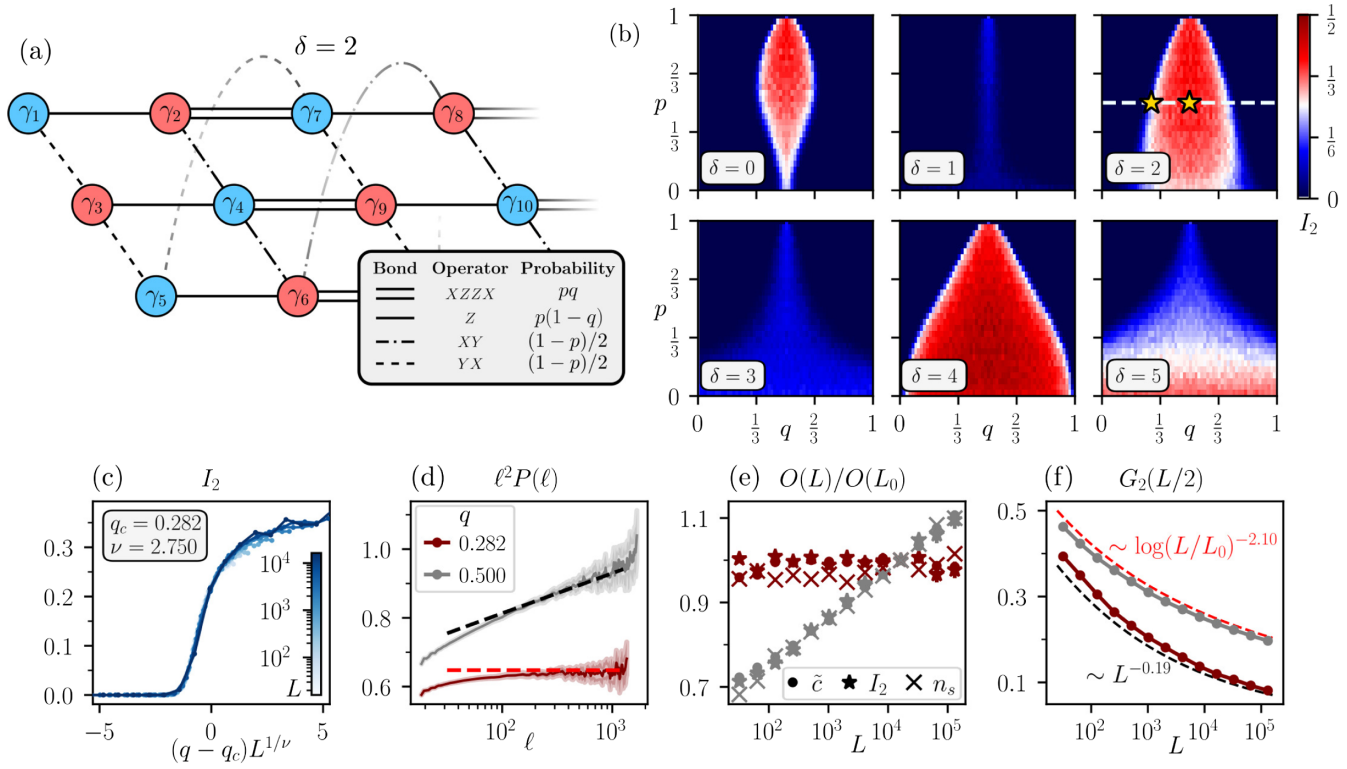

FIG. 12. Loop model for the $XZZX$ code. (a) Majorana lattice where each bond corresponds to an allowed parity check on the three-chain square lattice. The measurement probabilities for the different types of bonds and the corresponding Pauli operator on a single-qubit chain are shown in the legend and parametrized by $p, q \in [0, 1]$. Transverse boundary conditions defined by the twist δ correspond to connecting the first and third chains with bonds $\gamma_{(n,3)} \leftrightarrow \gamma_{(n+\delta,1)}$ (here, $\delta = 2$). (b) The phase diagram in the $p - q$ plane depicted via the mutual information I_2 at $L = 12288$ shown for different boundary twists δ. For even twists, the lattice is nonbipartite, and we observe an extended Goldstone phase (red). For odd twists, the lattice remains bipartite, and the worldlines are orientable such that no Goldstone phase is observed. Here, the mutual information is finite only when crossing $q = \frac{1}{2}$ or $p = 0$, corresponding to percolation criticality. (c)–(f) Entanglement and loop statistics with $\delta = 2$ along the dashed $p = \frac{1}{2}$ line in (b). (c) Scaling collapse of the two-interval mutual information I_2 near transition identifies the critical point $q_c \approx 0.282$ and correlation length exponent $\nu = 2.75$. (d) The steady-state stabilizer length distribution $P(\ell)$ reveals a logarithmic correction in the Goldstone phase compared to the conventional $P(\ell) \propto \ell^{-2}$ scaling at the transition. Dashed lines correspond to the universal value expected from CPLC in the Goldstone phase (black) and at the transition (red) [100]. (e) The system-size dependence of the mutual information I_2, fitted log-law coefficient $\tilde{c}$, and spanning number n_s, normalized against their magnitude at $L_0 = 2^{14}$, reveals logarithmic corrections in the Goldstone phase that are absent at the transition. (f) The two-leg watermelon correlator $G_2(L/2)$ exhibits power-law decay at the transition, with exponent $x_2 \approx 0.095$ consistent with that found in CPLC. Correlations decay more slowly in the Goldstone phase, falling off as $\log(L/L_0)^{-\alpha_2}$ with $\alpha_2 \approx 2.1$.

$p = 0$ corresponding exactly to δ copies of critical percolation. For δ even, we instead observe an extended Goldstone phase. When increasing δ, the parity measurements across the boundary of the ladder become longer in range and facilitate the onset of the Goldstone phase already at small measurement probabilities.

We show in Fig. 12(b) that turning on finite interchain coupling, i.e., breaking the orientability of the ladder, causes the percolation critical point to broaden into a critical fan, which is symmetric about $q = \frac{1}{2}$. Upon examination, we confirm that the entangled phase inside the fan is the Goldstone phase of CPLC. In the remainder of this section, we verify the universal behavior of CPLC for the particular case of $\delta = 2$.

A. Correlation length critical exponent

The scaling collapse of the mutual information I_2 along the dashed line at $p = \frac{1}{2}$ in Fig. 12(c) identifies the critical points $q_c = 0.282, 0.718$ (symmetric around $q = 0.5$) and the CPLC critical exponent $\nu = 2.75$.

B. Loop lengths

We define the length ℓ of a loop with respect to the indexing of the fermions on the lattice. The transition $q = q_c$ features conventional critical scaling $\ell^2 P(\ell) \to \alpha$, while the Goldstone phase exhibits logarithmic corrections $\ell^2 P(\ell) \to \beta \log(\ell)$ with both α and β being consistent with the CPLC values; see Fig. 12(d).

C. Entanglement growth

The loop distributions $P(\ell)$ readily imply the behavior for the entanglement entropy S_A and the mutual information $I_2(A,B)$ of contiguous subsystems of size $|A|,|B|$. We again take the ansatz $S_A(L) = [\tilde{c}(L)/3]\log_2[(L/\pi)\times \sin(\pi|A|/L)] + \text{const}$. At the critical points, $\tilde{c}$ and I_2 are constant in system size [see Fig. 12(e)], while a logarithmic correction is found in the Goldstone phase: $\tilde{c}, I_2 \propto \log(L)$. The numerical prefactors follow from $P(\ell)$ and are, thus, consistent with CPLC.

D. Purification

The Goldstone phase exhibits logarithmic corrections to purification, witnessed via the spanning number. In Fig. 12(e), we show the spanning number n_s at fixed circuit aspect ratio $T = L$, which remains constant at q_c but grows logarithmically with L in the Goldstone phase. The prefactor of the logarithmic growth is 0.14, comparable to $(1/2\pi) \approx 0.16$ expected from CPLC. See Appendix B for additional details on the dynamical purification and the spanning number.

E. Bulk critical exponents

Using the two-leg watermelon correlator $G_2(L/2)$, we extract bulk critical exponents at the critical point and in the Goldstone phase [see Fig. 12(f)]. At the transition, the results are consistent with $G_2(L/2) \sim L^{x_2}$, with exponent $x_2 \approx 0.095$. By contrast, we observe a logarithmic slowing down $G_2 \sim \log(L/L_0)^{-\alpha_2}$ with exponent $\alpha_2 \approx 2.1$ in the Goldstone phase. Both exponents are consistent with the results in the two-leg ladder and CPLC.

VI. CONCLUSION

Two-dimensional loop models represent a paradigm for a large class of solvable models in quantum and classical statistical mechanics. Using analytical arguments, confirmed by numerical simulations, we have strengthened the link between measurement-only Clifford circuits in $(1+1)$ dimensions and 2D loop models. Our work demonstrates that loop models provide a general framework which covers a large class of measurement-only circuits and measurement-induced phase transitions, including previously studied models as well as new types of setups considered here. Mapping circuits to loop models provides a means to classify the measurement-only evolution based on the symmetry and the topology of the corresponding loop model, as well as to analyze the universal long-wavelength behavior at measurement-induced phase transitions.

The loop model approach outlined in our work, in particular, the aspect of worldline orientability, provides a blueprint to study the rich phenomenology of 2D loop models with $(1+1)$-dimensional Clifford circuits. Promising routes may be the realization of exotic entangled states, such as topological phases or larger classes of nonunitary conformal field theories, which are both known to admit mappings to orientable loop models. The emergence of an entanglement transition with Ising universality at the tricritical point of the one-state Potts model stands as a particularly clear example of the diverse set of states and critical dynamics realizable by employing the loop model framework for quantum circuits.

Further exploring the link to loop models opens up a new perspective for general monitored quantum circuits. The question arises naturally whether it is possible to extend the loop model framework to include general unitary operations beyond discrete swap gates or non-Clifford measurements. For the former, the particular case of random Majorana gates has been shown to yield a similar nonlinear sigma model as the one that is obtained for CPLC [38,113]. Including non-Clifford measurements may similarly give rise to new braiding or fusion rules, which go beyond classical loop models. In both cases, orientability may emerge only on certain fine-tuned parameter values, while new symmetries may emerge which enlighten the connection of monitored circuits to quantum loop model approaches [123,187].

Based on the current work, an exciting future direction is the study of measurement-only circuits in higher dimensions and for different geometries. For instance, in two-dimensional circuits, the loop model and, in particular, its symmetries may be enriched by tunable geometries. An example of the latter is found in the 2D measurement-only Kitaev spin liquid [61,188], which gives rise to a tripartite Majorana graph. Adding higher-order Majorana measurements breaks this symmetry and makes the graph non-orientable, which leads to a peculiarly entangled Majorana liquid [61]. Exploring this scenario and generalizations with the loop model approach will help to establish a general classification of measurement-only circuits in higher dimensions beyond the currently established paradigms.

ACKNOWLEDGMENTS

We thank Joel Moore for fruitful discussions. K. K. was supported by a National Science Foundation Graduate Fellowship under Grant No. DGE 2146752 and by the U.S. Department of Energy, Office of Science, National Quantum Information Science Research Centers, Quantum Science Center. M. B. acknowledges support from the Deutsche Forschungsgemeinschaft (DFG, German Research Foundation) under Germany's Excellence Strategy Cluster of Excellence Matter and Light for Quantum Computing (ML4Q) EXC 2004/1 390534769 and by the DFG Collaborative Research Center (CRC) 183 Project No. 277101999-project B02.

APPENDIX A: NUMERICAL METHOD FOR MAJORANA CIRCUITS

Whereas a stabilizer state in a generic Clifford circuit requires an $O(L^2)$ tableau representation, the current state

of a Gaussian Majorana circuit is represented by the $O(L)$ pairings corresponding to the end points of worldlines. Moreover, while the computational cost of a projective measurement generally scales as $O(L^3)$ for stabilizer states, measurements in a loop model require only $O(1)$ operations to rearrange the pairings. These computational benefits are further enhanced by efficient schemes for generating deeper circuits via shuffling and concatenating shallower circuits [100]. By generating a "pool" of N shallow circuits (e.g., a single layer), repeated shuffling and concatenation of the elements doubles the circuit depth with every round of concatenation. Then reaching a circuit depth T for L qubits in a pool of size N requires computational cost that scales as $\mathcal{O}[NL\log_2(T)]$. As a result, one can efficiently simulate system sizes several orders of magnitude greater than is possible with stabilizer states. This is crucial for accurately identifying logarithmic scaling corrections which are otherwise challenging to distinguish from anomalous power-law scaling.

1. Entanglement statistics from the boundary-loop distribution

Given a circuit trajectory with periodic boundary conditions (PBCs), we might ask for an entanglement measure averaged over all translations of the system in order to extract maximal information out of the state. In this case, one can equivalently take the distribution $P(\ell)$ of open loops with both ends on the final $t = T$ temporal boundary, reducing the number of computations which need to be performed in each trajectory. Here, we give a short review of how this is implemented.

Let A and B be two *disjoint* subsystems for which we would like to compute the ensemble averaged mutual information $\langle\langle I_2(A,B)\rangle\rangle$. This can be done via the sum

$$I_2(A,B) = \frac{1}{2}\sum_{x\in A}\sum_{y\in B} P[\ell = \mathrm{dist}(x,y)], \qquad \text{(A1)}$$

where the distance function respects the PBC such that

$$\mathrm{dist}(x,y) = \min(|x-y|, N-|x-y|)$$

and the factor of $1/2$ accounts for the directionality of the distance function. Without loss of generality, let $A = [1,|A|]$ and $B = [|A|+\Delta+1, |A|+\Delta+|B|]$ with $|A|, |B| \le N/2$ and $\Delta \le N-|A|-|B|$ so that the intervals remain disjoint. We then always have $y > x$ for $y\in B$ and $x\in A$, allowing us to write the distance function instead as

$$\mathrm{dist}(x,y|y>x) = \begin{cases} y-x & y-x \le N/2, \\ N-(y-x) & \text{else.} \end{cases}$$

In practice, the double sum over coordinates is inefficient when going to very large system sizes. This can be simplified by instead expressing the mutual information as

$$I_2(A,B) = \sum_{x\in A, y\in B} P[\ell = \mathrm{dist}(x,y)] = \sum_{\ell=1}^{N/2} P(\ell) w_{A,B}(\ell),$$

where the weight function $w_{A,B}(\ell)$ depends on the partitions A and B only via $|A|$ and $|B|$ and Δ and can be written explicitly as

$$w_{A,B}(\ell) = \frac{1}{2}\sum_{x\in A, y\in B} \delta_{\ell,\mathrm{dist}(x,y)}.$$

We now give explicit derivation of $w(\ell)$ for two cases: (i) the computation of I_2 and (ii) the computation of S_ℓ.

a. Weight function for two-interval mutual information

Recall that throughout the main text we compute the mutual information I_2 between regions $A = [1, N/8]$ and $B = [1+N/4, 3N/8]$ such that $|A| = |B| = \Delta = N/8$. From this choice, the distance function is always given simply by $y - x$. Letting $y = z + 2|A|$, we can evaluate the weight function

$$\begin{aligned} w(\ell) &= \frac{1}{2}\sum_{x=1}^{|A|}\sum_{z=1}^{|A|} \delta_{\ell,2|A|+z-x} \\ &= \frac{1}{2}(|A| - |2|A| - \ell|)\Theta(|A| - |2|A| - \ell|), \end{aligned} \qquad \text{(A2)}$$

where $\Theta(\cdot)$ is the step function. This gives exactly the number of positions $x\in A$ such that a loop of length ℓ terminates at some $y = x + \ell \in B$. Then, to compute the ensemble-averaged entanglement entropy, we can simply compute the weighted sum

$$\langle\langle I_2(A,B)\rangle\rangle = \sum_\ell P(\ell) w(\ell)$$

using the loop length distribution obtained from averaging over many trajectories.

b. Weight function for the subsystem entanglement

While a single computation such as I_2 is generally inexpensive, it becomes quite costly if one wants the subsystem entanglement entropy S_ℓ for all allowed subsystem sizes ℓ. As such, it is useful to seek an efficiently computable expression for $w(\ell)$. Let us now take subsystem $A = [1,|A|]$ and its complement $\overline{A} = [|A|+1, N]$ for $|A| \le N/2$. It is no longer generically true that $y - x \le N/2$ for $y\in\bar{A}$ and $x\in A$, and so some additional care is required. For fixed $x\in A$, the distance function switches behavior at $y^* = (N/2) - |A| + x \ge 1$. We can then split the sum over y and evaluate $w(\ell)$ as follows:

$$w(\ell) = \frac{1}{2}\sum_{x=1}^{|A|}\sum_{z=1}^{N-|A|}\delta_{\ell,\mathrm{dist}(x,|A|+z)} = \frac{1}{2}\sum_{x=1}^{|A|}\left[\sum_{z=1}^{z^*}\delta_{\ell,|A|+z-x} + \sum_{z=z^*+1}^{N-|A|}\delta_{\ell,N-|A|-z+x}\right] = \begin{cases}\min(\ell,|A|) & 1\le\ell<N/2\\ N/2 & \ell=N/2.\end{cases} \tag{A3}$$

Then the ensemble-averaged entanglement entropy for a contiguous subsystem of $|A|=\ell$ Majoranas is

$$\langle\langle S_\ell\rangle\rangle = \frac{N}{2}P(N/2) + \sum_{\ell'=1}^{\ell-1}\ell' P(\ell') + \sum_{\ell'=\ell}^{N/2-1}\ell P(\ell').$$

While this eliminates one sum (and many calculations from each trajectory), it is still cumbersome to do $O(N^2)$ calculations to compute $\langle\langle S_\ell\rangle\rangle$ for all ℓ. This can be simplified by observing a recursive structure with respect to ℓ. In particular, we have

$$\langle\langle S_{\ell+1}\rangle\rangle = \langle\langle S_\ell\rangle\rangle + \sum_{\ell'=\ell+1}^{N/2-1}P(\ell').$$

Now let us define a slightly modified cumulative density function for the loop length distribution:

$$F(\ell) \equiv \sum_{\ell'=\ell}^{N/2-1}P(\ell'),$$

such that $F(1) = 1 - P(N/2)$. Then we can write the following recursive relations:

$$F(\ell+1) = F(\ell) - P(\ell),$$
$$\langle\langle S_{\ell+1}\rangle\rangle = \langle\langle S_\ell\rangle\rangle + F(\ell+1).$$

Equipped with the above, the full set of $\langle\langle S_\ell\rangle\rangle$ can be computed from the loop length distribution $P(\ell)$ in $\mathcal{O}(N)$ time without any computation during individual trajectories.

c. Watermelon correlators

In principle, the watermelon correlator $G_2(x,y)$ can be extracted from the ensemble-averaged loop length distribution $P(\ell)$. However, in practice, this is quite cumbersome as we outline below. Given a circuit of depth T, let $P(\ell)$ be the distribution of boundary loops on the final time boundary, assuming that we impose fixed boundary conditions at $t=0$ (i.e., a pure initial state). For $x=(l,T)$ and $y=(m,T)$, $G_2(x,y)$ gives the probability that x and y lie along the same loop in the *bulk* of a loop model. Taking two copies of the circuit, we can glue the open ends together in order to close all of the loops. Then $G_2(x,y)$ is the probability that points l and m on the boundary of the circuit are connected by a loop when these two copies of the circuit are glued together. A closed loop formed by the gluing consists of alternating arcs from the two copies, with the number of arcs in the path being between 2 and $2N$. The probability of l and m being on the same loop can be decomposed into a sum over the probability of connecting ℓ and m with a path of fixed number of arcs:

$$G_2(l,m) = \sum_{i=1}^{N}\mathrm{Prob}(l\leftrightarrow m|2i\mathrm{arcs}) \equiv \sum_{i=1}^{N}\mu_i(l\leftrightarrow m).$$

For example, the first-order term μ_i is simply given by $P(|l-m|)^2$. Higher-order terms can be further broken into a sum over the length of the two halves of the path (i.e., $l\to m$ and $m\to l$). In general, there are an exponential number of possible paths, making the calculation of $G_2(l,m)$ from $P(\ell)$ intractable. Of course, many such paths have negligible weight and could be excluded from the sum, but this remains impractical. As such, all values of G_2 reported in this work are computed in *each* trajectory rather than from the ensemble-averaged length distribution $P(\ell)$.

APPENDIX B: DYNAMICAL PURIFICATION TIMESCALE

As we note throughout the main text, in the Goldstone phase there are logarithmic corrections to the dynamics which can be observed via the spanning number $n_s(t,L)$. In Figs. 9(c) and 12(e), we show for a fixed circuit aspect ratio that the spanning number $n_s(t=L,L)$ grows logarithmically with the system size. As noted in Ref. [100], for unit aspect ratio ($t=L$) the spanning number should be given exactly by the renormalized spin stiffness of the $O(n=1)$ loop model at RG scale $t=L$. This result can be readily extended to generic aspect ratio. At RG scale Λ, the renormalized spin stiffness is given to leading order by $\tilde{K}(\Lambda) = (1/2\pi)\log(\Lambda/\Lambda_0)$. As a result, we expect the spanning number in the Goldstone phase to evolve as

$$n_s(t,L) \sim F\left(\frac{t}{L}\frac{2\pi}{\log(L/L_0)}\right) \tag{B1}$$

for some scaling function F. In the circuit language, this corresponds to a slowing of purification such that the typical timescale over which a maximally mixed state is purified now depends on system size as $L\log(L)$ rather than L.

In Fig. 13, we show the time evolution of the spanning number in the three-leg ladder at the two marked points from Fig. 12(b). At the transition $q=q_c$, we observe conventional critical purification with dynamical exponent $z=1$ such that $n_s(t,L)=F(\tau=t/L)$. Equivalently, this can be considered as the $L_0\to 0$ limit of Eq. (B1). In the

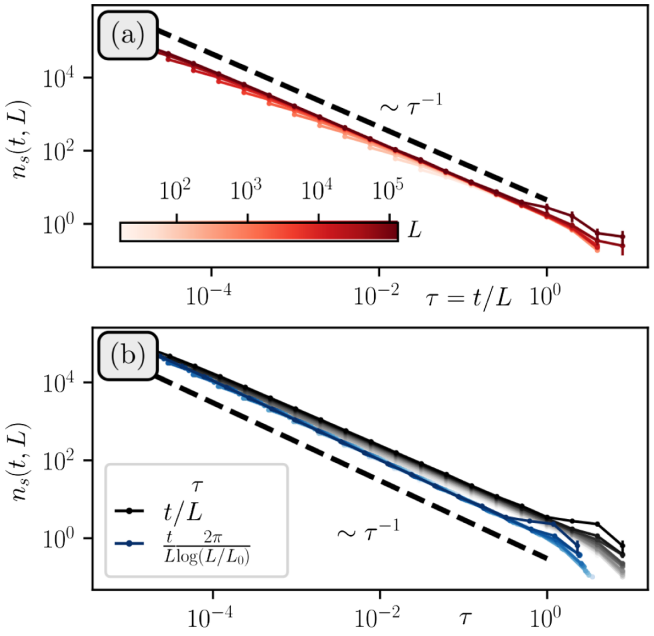

FIG. 13. Evolution of the spanning number $n_s(t,L)$ in the three-leg ladder at the marked points in Fig. 12(b). (a) The transition at $p=\frac{1}{2}$, $q=q_c=0.282$ has conventional critical behavior with dynamical exponent $z=1$. This is reflected by the spanning number collapsing to a single curve parametrized by rescaled time $\tau=t/L$. While $n_s>1$, purification gives $n_s\propto\tau^{-1}$, as shown by the black dashed line. (b) In the Goldstone phase at $p=q=\frac{1}{2}$, logarithmic corrections modify the purification dynamics. Here, we show $n_s(t,L)$ for two different rescaled times τ. Conventional $z=1$ scaling with $\tau=t/L$ (gray) does not capture the logarithmic corrections. Accounting for the renormalized spin stiffness by taking $\tau=[2\pi t/L\log(L/L_0)]$ with $\log(L_0)=-5$ yields excellent data collapse.

Goldstone phase, at $q=\frac{1}{2}$, the logarithmic corrections lead to finite L_0 being required for scaling collapse of the spanning number. For this particular example, we find $\log(L_0)=-5$, which implies that logarithmic corrections are non-negligible for $L\gtrsim 10^2$.

For small system sizes, these logarithmic corrections to purification can be difficult to unambiguously identify. Indeed, a naive rescaling as $n_s(t,L)\sim F[tL^{-z^*}]$ in the regime $n_s\gtrsim 1$ would suggest an anomalous scaling exponent $z^*\approx 1.1$.

APPENDIX C: EFFECTIVE TRANSFER MATRIX FOR INTERACTING MAJORANA CIRCUITS

In this section, we derive an effective transfer matrix description for the family of orientable, interacting Majorana circuits considered in Sec. III B.

1. Measurement-only *XXZ* chain

Let us consider the decoupled limit of the two-leg ladder (XY and YX) perturbed by four-fermion (ZZ) measurements. Moreover, let us impose a brick-wall structure such that the circuit consists of alternating layers of two-qubit bricks. The two types of layers are given identical probabilities for measuring the different operators: $p_{XY}=p_{YX}=sp/2$, $p_{ZZ}=s(1-p)$, and $p_{\mathbb{1}}=1-s$. The transfer matrix for this circuit can be written as

$$\hat{T}=\hat{T}_1\hat{T}_2=\left(\prod_{j=1}^{\lfloor L/2\rfloor}T_{2j-1}\right)\left(\prod_{j=1}^{\lfloor L/2\rfloor}T_{2j}\right),$$

$$T_l=(1-s)\mathbb{1}+\frac{sp}{2}(\mathcal{P}_{XY}+\mathcal{P}_{YX})+s(1-p)\mathcal{P}_{ZZ},$$

where T_l is the transfer matrix corresponding to a brick acting on qubits l and $l+1$. The projectors $\mathcal{P}_{X_lY_{l+1}}$ and $\mathcal{P}_{Y_lX_{l+1}}$ individually form the generators of a TL algebra which we denote e_l and f_l, respectively. For forced projections onto the $+1$ outcome, we may write $\mathcal{P}_{Z_lZ_{l+1}}=\mathbb{1}_{l,l+1}+2\mathcal{P}_{X_lY_{l+1}}\mathcal{P}_{Y_lX_{l+1}}-\mathcal{P}_{X_lY_{l+1}}-\mathcal{P}_{Y_lX_{l+1}}$. Averaging over the possible two-qubit states, a forced projection onto the $+1$ eigenstate of Z_lZ_{l+1} followed by normalization of the wave function may be approximated as $\mathcal{P}_{Z_lZ_{l+1}}\to 1-e_l-f_l+2e_lf_l$. The transfer matrix then takes the form

$$T_l=[1+s(1-2p)]\mathbb{1}+\frac{s(3p-2)}{2}(e_l+f_l)+2s(1-p)e_lf_l.$$

Observe that the set $\{E_l\equiv e_lf_l\}$ generates a TL algebra. When $p=\frac{2}{3}$, the transfer matrix involves only this new set of generators:

$$T_l|_{p=2/3}=\left(1-\frac{s}{3}\right)\mathbb{1}+\frac{2s}{3}E_l.$$

Since the odd and even layers of the circuit have the same measurement probabilities, this corresponds to a critical one-state Potts model with TL algebra generators E_l. Then one can identify $p_c=\frac{2}{3}$ as a strong-coupling fixed point, in agreement with the numerical results presented in Sec. II E.

a. Competing four-fermion measurements

Let us now consider adding XIX measurements which compete with the other four-fermion ZZ measurements. This generally spoils the previous solution for a strong-coupling fixed point. Nonetheless, suppose we now take $r_{ZZ}\neq 1$. The circuit must now involve three-qubit bricks, each of which has a transfer matrix like

$$T_l\sim(1-s)\mathbb{1}+\frac{sp}{2}(\mathcal{P}_{XY}+\mathcal{P}_{YX})+s(1-p)(r\mathcal{P}_{ZZ}+(1-r)\mathcal{P}_{XIX}).$$

As before, we may effectively write $\mathcal{P}_{X_l X_{l+2}} \sim \mathbb{1} - e_l - f_{l+1} + 2e_l f_{l+1}$. Then, writing the transfer matrix in terms of the TL generators, we have

$$T_l \sim \frac{1-sp}{s}\mathbb{1} + \frac{3p-2}{2}e_l + \frac{p-2(1-p)r}{2}f_l - (1-p)(1-r)f_{l+1} + 2(1-p)e_l((1-r)f_{l+1} + rf_l).$$

As before, the coefficient on e_l vanishes for $p = 2/3$. Now, however, there remains finite magnitude of f_i and f_{i+1}. Letting $p = \frac{2}{3} + \delta$, the two terms become $(1 - r/3) + \delta(r + \frac{1}{2})$ and $(1 - r/3) - \delta(1 - r)$. We see that these deviate from $(1 - r)/3$ in opposite directions. They take on equal and opposite magnitude at $p_c(r) = 2(1 - 2r)/(1 - 4r)$, which falls in the interval $[0, 1]$ for $r \in [1/2, 1]$. Since the phase diagram must be symmetric under $r \to 1 - r$, up to the presence of edge modes, in the interval $r \in [0, 1/2]$ we have a phase boundary at $p_c(r) = 2(1 - 2r)/(3 - 4r)$. This is in agreement with the phase diagram obtained from numerical simulation, shown by the black dashed line in Fig. 8(c).

This argument can be made more precise by considering a full row transfer matrix:

$$T \sim \sum_l \left[\frac{s}{2}(\mathcal{P}_{X_l Y_{l+1}} + \mathcal{P}_{Y_l X_{l+1}}) + (1-s)r\mathcal{P}_{Z_l Z_{l+1}} + (1-r)\mathcal{P}_{X_l X_{l+2}}\right].$$

It is now useful to take the XY and YX measurements to be forced projections onto $+1$ and -1 on opposite sublattices such that $e_{2l-1} = \mathcal{P}_{X_{2l-1}Y_{2l}}$ while $e_{2l} = \mathbb{1} - \mathcal{P}_{X_{2l}Y_{2l+1}}$. Then forcing ZZ and XIX measurements onto the $+1$ outcome gives

$$T = \sum_l [\lambda(e_l + f_l) + 2[re_l f_l - (1-r)e_l f_{l+1}]] = \sum_l [\lambda(e_l + f_l) + e_l(\delta r(f_l + f_{l+1}) + (f_l - f_{l+1}))],$$

where we define $\lambda = [s/2(1-s)] - |\delta r|$ and $\delta r = 2r - 1$. We see that, for $s_c(r) = 2|\delta r|/(1 + 2|\delta r|)$, the linear term vanishes (i.e., $\lambda = 0$), leaving only the couplings $e_l f_l$ and $e_l f_{l+1}$. While we cannot construct a TL algebra from this mixture, we retain a well-defined continuum limit. Identifying ϵ and $\bar{\epsilon}$ as the energy-density fields in the conformal field theory for e_l and f_l, respectively, the coupling generally takes the form $\epsilon(2\delta r\bar{\epsilon} - \partial_x\bar{\epsilon})$. A shift in the coordinates for $\bar{\epsilon}$ then reduces the coupling to simply $2\delta r\epsilon\bar{\epsilon}$ so that the effective long-wavelength description of the circuit is simply that of the earlier interacting circuit but with a modified interaction strength.

APPENDIX D: BROADENING OF THE PERCOLATION CRITICAL POINT FOR NON-GAUSSIAN CIRCUITS

As noted in Sec. III B, when the area-law phases in the Gaussian and interacting limits of a circuit are not topologically equivalent, then there must be an entanglement transition observed upon varying the interaction strength. Moreover, since four-fermion measurements are irrelevant in a short-loop phase, this transition ought to occur at *finite* interaction strength $0 < s_c < 1$. To see this, consider the Gaussian limit drawn from orientable subset $\mathcal{O}_3$ but excluding YY measurements. Here, XX measurements drive the otherwise decoupled critical chains into an area-law phase. Let us now perturb this circuit with

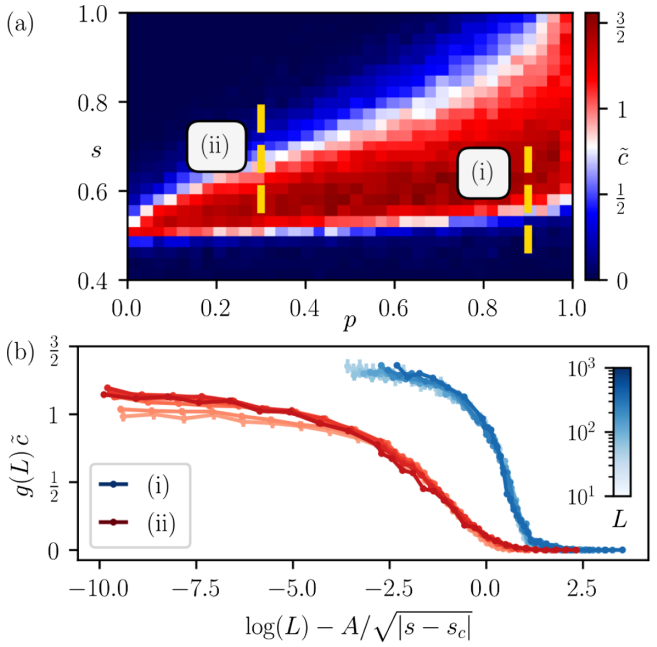

FIG. 14. Broadening of the percolation critical point for non-Gaussian circuits. Here, we take $r_{XX} = 1$, $r_{ZZ} = 1$, and $q = \frac{1}{2}$. (a) Phase diagram showing the log-law coefficient $\tilde{c}$ in the $s - p$ plane shows an extended critical phase separating two topologically distinct area-law phases. The transitions terminate at an interacting percolation critical point at $(p, s) = (0, 1/2)$, a decoupled critical point at $(p, s) = (1, 0)$, and a BKT critical point at $(p, s) = (1, 2/3)$. Data shown are extracted from the subsystem entanglement entropy S_ℓ for system size $L = 256$. (b) Scaling collapse of the log-law coefficient $\tilde{c}$ from fitting the subsystem entanglement profile S_ℓ for the two cuts along the transition marked in (a). The scaling is consistent with a sudden jump in $\tilde{c}$ at a BKT transition such that $g(L)\tilde{c} = F(x)$ for $g(L) = [1 + (2\log(L) - B)^{-1}]^{-1}$ and F a function of $x = \log(L) - A/\sqrt{|s - s_c|}$. Cut (i) is taken at $p = 0.9$, showing the BKT transition at $s_c \approx 0.628$ from the interacting area-law phase at $s < s_c$ to the critical phase, with fitting parameters $A \approx 1.5$ and $B \approx -9.5$. Cut (ii) is taken at $p = 0.3$, showing the BKT transition from the Gaussian area-law phase to the critical phase at $s_c \approx 0.563$, with fitting parameter $A \approx 2.35$ and $B \approx 5.41$.

orientable non-Gaussian four-fermion ZZ measurements such that the interacting limit lies also in an area-law phase. We take measurement probabilities $p_{XY} = p_{YX} = sp/2$, $p_{XX} = s(1-p)$, and $p_{ZZ} = 1-s$. Upon varying the interaction strength, we observe an extended critical phase $s_{c,1} < s < s_{c,2}$ separating the two topologically distinct area-law phases. The transitions from either area-law phase into the critical phase falls into the BKT universality class, as reflected in Fig. 14(b).

The apparent broadening of the transition into a critical phase can be well understood by varying not only the interaction strength, but also the strength of the interchain XX measurements which are responsible for inducing an area law in the Gaussian limit. As shown in Fig. 14(a), the decoupled critical point at $p = 1$ is robust against finite interactions, which are RG irrelevant, giving an extended critical phase. For weak interchain coupling $1-p \ll 1$, the measurement frustration with ZZ measurements suppresses the effect of XX measurements, effectively protecting the criticality of the decoupled limit. In the opposing limit ($p = 0$), ZZ and XX measurements reduce to two decoupled copies of the repetition code which undergo a percolation transition at $s = 1/2$. Here, XY and YX measurements appear as higher-order interaction coupling between two chains at the percolation critical point, leading again to a broadening. The now-broadened critical points near $p = 0, 1$ extend to two BKT lines that span the two limits. In the intermediate critical phase, the entanglement entropy has log-law coefficient $\tilde{c} \approx \frac{3}{2}$.

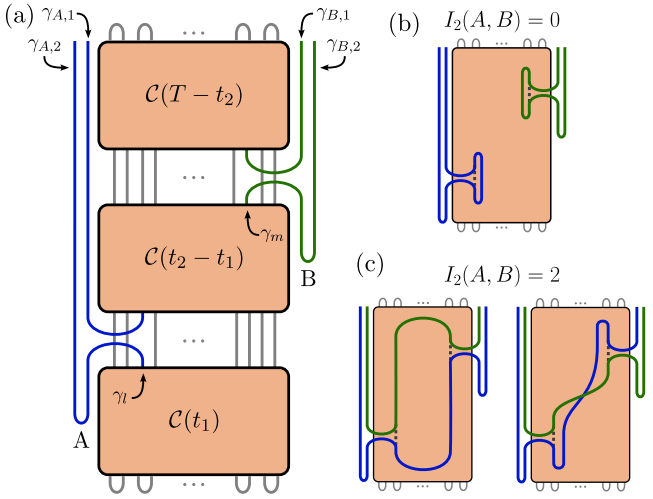

FIG. 15. Measuring bulk correlations in the circuit. We present an ancilla-based scheme for detecting the two-leg watermelon correlator $G_2(x,y)$ with $x = (l,t_1)$ and $y = (m,t_2)$. (a) Between times $t = 0$ and $t = t_1$, an initial state ρ_0 is evolved by a circuit $\mathcal{C}$. At time t_1, a parity measurement pairs the bulk worldline γ_l with worldline $\gamma_{A,1}$ from ancilla A (blue). The circuit then evolves to time t_2, when γ_m is paired with $\gamma_{B,1}$ from ancilla B (green), after which the circuit evolves to the final time $T \gtrsim L$. (b),(c) $G_2(x,y)$ is the probability that (x,t_1) and (y,t_1) are on the same, closed loop, i.e., $G_2(x,y) = \frac{1}{2}I_2(A,B)$ the mutual information between the ancillas. When no worldlines connect the two points, (b) $I_2(A,B) = 0$ and otherwise $I_2(A,B) = 2$; see possible examples in (c).

APPENDIX E: ANCILLA PROBES OF BULK CORRELATION FUNCTIONS

In order to extend the set of accessible observables from *boundary* to *bulk* correlations of the loop model, the knowledge of the final state at the temporal boundary is no longer sufficient, and one needs to access information along the whole of the circuit trajectory. Here, we introduce an ancilla-based detection scheme [34], with which n-particle bulk correlation functions, i.e., the watermelon correlators $G_k(x,y)$ introduced in Sec. II, can be measured in the Majorana circuit.

We consider the two-leg watermelon correlator $G_2(x,y)$, which measures the probability that two points x and y lie upon a single, *closed* loop in the two-dimensional plane. In the circuit, this translates to the probability that two Majorana modes $\gamma_l(t_1)$ and $\gamma_m(t_2)$ at spacetime points $x = (l,t_1), y = (m,t_2)$ share a closed loop. In order to detect $G_2(x,y)$ in the circuit, we prepare two additional pairs of ancillary worldlines, A and B, with $A = (\gamma_{A1},\gamma_{A2})$ and $B = (\gamma_{B1},\gamma_{B2})$, as depicted in Fig. 15. Both are put in a parity eigenstate at $t = 0$, $i\langle\gamma_{A1}(0)\gamma_{A2}(0)\rangle = i\langle\gamma_{B1}(0)\gamma_{B2}(0)\rangle = 1$. Now we evolve the circuit over time but interrupt it at times $0 \ll t_1, t_2 \ll T$, when the parities $\gamma_{A1}(t_1)\gamma_l(t_1)$ and $\gamma_{B1}(t_2)\gamma_m(t_2)$ are measured. This inserts the marked loops in Fig. 15 into the bulk while storing the history of the loops crossing through spacetime points x and y in ancilla worldlines γ_{A2} and γ_{B2}, respectively.

Only if the Majoranas $\gamma_l(t_1)$ and $\gamma_m(t_2)$ share a closed loop without inserting the ancilla measurements are A and B connected via exactly two distinct worldlines. Otherwise, no worldlines connect A and B. Thus, $G_2(x,y)$ gives precisely the mutual information between the two ancillas, $G_2(x,y) = \frac{1}{2}I(A,B)$. Higher-order watermelon correlators $G_k(x,y)$ can be constructed analogously by making use of further ancilla states. Notably, $G_2(x,y)$ appears as an out-of-time order correlator in the Majorana framework. The mutual information becomes the time-nonlocal (connected) correlation function $\langle\gamma_{A1}(0)\gamma_{A1}(T)\gamma_{B1}(0)\gamma_{B1}(T)\rangle - \langle\gamma_{A1}(0)\gamma_{A1}(T)\rangle\langle\gamma_{B1}(0)\gamma_{B1}(T)\rangle$.

APPENDIX F: SUPPLEMENTARY DATA FOR ISING TRANSITION

In Sec. III B 2 in the main text, we identify a measurement-induced transition at the tricritical point of the one-state Potts model, for which the correlation length exponent $\nu \approx 1$ is consistent with Ising universality. Here, we provide additional characterization of the transition, examining both the critical exponents and the prefactor $\tilde{c}$ for the logarithmic entanglement scaling.

1. Critical exponents η and $\eta_\parallel$

To further verify the Ising universality of the transition, we employ ancilla probes to extract the bulk critical exponent η and the surface critical exponent $\eta_\parallel$. For Ising universality realized via the two-state Potts model, we expect $\eta = \frac{1}{4}$ and $\eta_\parallel = 1$ [155]. As with watermelon correlators, these exponents can be determined by examining the mutual information between ancillas which are entangled with the system [34]. In particular, we take PBC and evolve the bulk system under measurement-only dynamics until time t_0. We then maximally entangle qubit 1 with ancilla A and qubit $\lfloor L/2 \rfloor + 1$ with ancilla B. From the subsequent time evolution of the mutual information $I_2(t, L)$ between the ancilla, we extract exponents by scaling collapse of the form $I_2(t, L) \sim L^a F[(t - t_0)/L]$. For $a = \eta, \eta_\parallel$ we take $t_0 = 3L, 0$, respectively.

The rescaled mutual information is shown in Fig. 16, from which we obtain $\eta \approx 0.23$ and $\eta_\parallel \approx 1.11$. These are comparable to the expected values for the Ising and two-state Potts model, with $\eta_\parallel$ being unambiguously distinct from the percolation value $\eta_\parallel^{(\mathrm{perc})} = 2/3$.

The uncertainty in the trajectory-averaged mutual information can be reduced by instead entangling groups of N_A ancilla to the bulk system again in the regions surrounding $x = 1$ and $y = \lfloor L/2 \rfloor + 1$. As with the $N_A = 1$ case, this inserts $2N_A$ marked loops at both bulk regions. For sufficiently large system sizes and late times, the ancilla mutual information is dominated by the largest watermelon correlator. As such, the scaling collapse reveals η and $\eta_\parallel$. Taking $N_A > 1$ has the added advantage of eliminating possible issues where certain sites or Majoranas live in decoupled sectors, which can lead to spurious results with $N_A = 1$. For $N_A = 2, 4$ we find similar results as for $N_A = 1$, with the estimated value for $\eta_\parallel$ more closely approaching 1 for larger N_A.

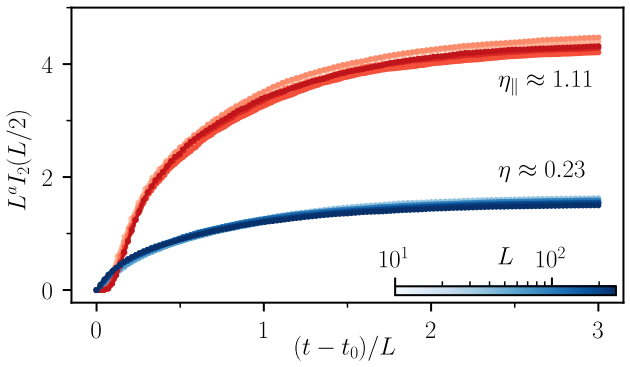

FIG. 16. Ancilla probes for Ising criticality. Evolution of the mutual information I_2 between an ancilla coupled to the system at separation $L/2$ at time t_0. For the bulk exponent $a = \eta$, we take $t_0 = 2L$ and find $\eta \approx 0.25$, consistent with the expected $\eta = \frac{1}{4}$ for Ising universality. For the surface exponent $a = \eta_\parallel$, we take $t_0 = 0$, finding $\eta_\parallel \approx 1.1$, comparable to the Ising value $\eta_\parallel = 1$.

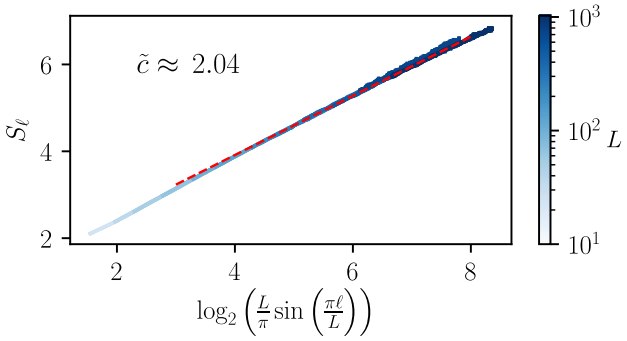

FIG. 17. Log-law scaling at the Ising transition. At the Ising transition, the entanglement entropy S_ℓ for all system sizes L falls onto a single line when taken against $\log_2[\sin(\pi\ell/L)L/\pi]$. The slope identifies the log-law coefficient $\tilde{c} \approx 2.04$ when fitted against all data for $L > 100$.

2. Enhanced logarithmic entanglement scaling

As noted in the main text, the coefficient $\tilde{c}$ for the log-law entanglement scaling observed at the measurement-induced Ising transition is much larger than the conventional $c = \frac{1}{2}$. As shown in Fig. 17, the subsystem entanglement entropy shows a clear log-law scaling behavior consistent with $\tilde{c} = 2$.

APPENDIX G: SUPPLEMENTARY DATA FOR INTERACTION-INDUCED GOLDSTONE PHASE

Here, we provide supplementary data for the scenario discussed in Sec. III D 2 wherein nonorientable four-fermion measurements perturbing an otherwise orientable Gaussian circuit induce a CPLC Goldstone phase. Starting from the Gaussian circuit defined by orientable set $\mathcal{O}_3$, we introduce non-Gaussian measurements of the Pauli operator ZXY. This four-fermion operator is incompatible with the worldline orientations fixed by the Gaussian measurements. Let the measurement probabilities be $p_{XX} = p_x^2$, $p_{YY} = p_y^2$, $p_{XY} = p_{YX} = p_x p_y$, and $p_{ZXY} = 1 - p$, where $p_x \equiv pq$ and $p_y \equiv p(1 - q)$. As shown in Fig. 18(a), finite measurement rate for the nonorientable, non-Gaussian ZXY operator yields an entangled phase fanning out from the vicinity of the maximally frustrated Gaussian point $(p, q) = (1, 1/2)$. At sufficiently large interaction strength, the fact that ZXY operators are not all mutually commuting leads to a volume-law phase, as seen for other circuits with incommensurate four-fermion interactions. For weaker interaction strength, the interaction-induced entangled phase resembles the CPLC Goldstone phase. At the transitions, we find correlation length exponent $\nu \approx 2.75$ and $\tilde{c} \sim$ const, as shown in Figs. 18(b) and 18(c). Moreover, between the two critical lines, we observe an

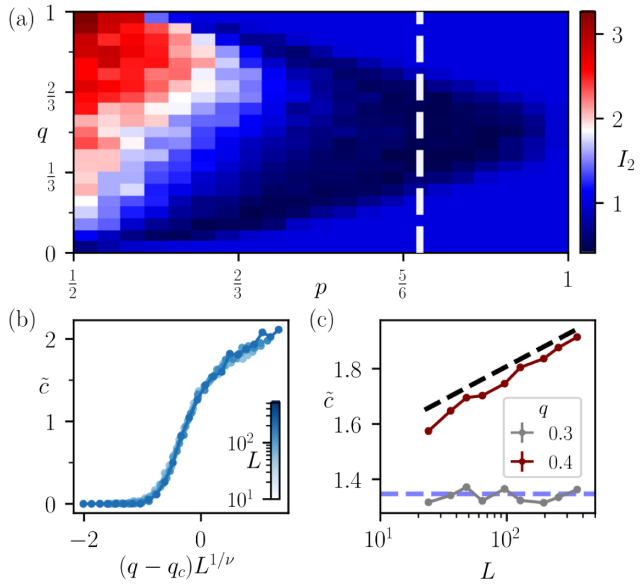

FIG. 18. Interaction-induced CPLC Goldstone phase. Entanglement statistics in the Gaussian circuit on orientable operators $\mathcal{O}_3$ is perturbed by measurements of the nonorientable four-fermion operator ZXY. (a) Phase diagram in the $p-q$ plane showing an entangled phase which emerges with sufficient interaction strength and measurement frustration. (b) Scaling collapse of $\tilde{c}$ near the transitions along the dashed line marked in (a) reveals the critical point $q_c \approx 0.305$ and is consistent with the correlation length exponent $\nu = 2.75$ expected from CPLC. (c) Scaling of the log-law coefficient $\tilde{c}$ with respect to system size L at the transition (gray) and in the intermediate entangled phase (maroon) along the dashed line at $p = 0.85$ in (a). The black and blue dashed lines correspond to the expected scaling of $\tilde{c}$ for the CPLC Goldstone phase and transition, respectively.

apparent logarithmic correction to entanglement entropy which is consistent with CPLC [see Fig. 18(c)]. This provides compelling evidence that breaking worldline orientability, even if only at the four-fermion level, leads to CPLC physics.

[1] J. Preskill, *Quantum computing in the NISQ era and beyond*, Quantum **2**, 79 (2018).

[2] S. Ebadi *et al.*, *Quantum optimization of maximum independent set using Rydberg atom arrays*, Science **376**, 1209 (2022).

[3] A. Erhard, H. P. Nautrup, M. Meth, L. Postler, R. Stricker, M. Stadler, V. Negnevitsky, M. Ringbauer, P. Schindler, H. J. Briegel, R. Blatt, N. Friis, and T. Monz, *Entangling logical qubits with lattice surgery*, Nature (London) **589**, 220 (2021).

[4] L. Postler, S. H. en, I. Pogorelov, M. Rispler, T. Feldker, M. Meth, C. D. Marciniak, R. Stricker, M. Ringbauer, R. Blatt, P. Schindler, M. Müller, and T. Monz, *Demonstration of fault-tolerant universal quantum gate operations*, Nature (London) **605**, 675 (2022).

[5] R. Stricker, D. Vodola, A. Erhard, L. Postler, M. Meth, M. Ringbauer, P. Schindler, T. Monz, M. Müller, and R. Blatt, *Experimental deterministic correction of qubit loss*, Nature (London) **585**, 207 (2020).

[6] D. Nigg, M. Müller, E. A. Martinez, P. Schindler, M. Hennrich, T. Monz, M. A. Martin-Delgado, and R. Blatt, *Quantum computations on a topologically encoded qubit*, Science **345**, 302 (2014).

[7] S. Krinner, N. Lacroix, A. Remm, A. D. Paolo, E. Genois, C. Leroux, C. Hellings, S. Lazar, F. Swiadek, J. Herrmann, G. J. Norris, C. K. Andersen, M. Müller, A. Blais, C. Eichler, and A. Wallraff, *Realizing repeated quantum error correction in a distance-three surface code*, Nature (London) **605**, 669 (2022).

[8] C. Ryan-Anderson, J. G. Bohnet, K. Lee, D. Gresh, A. Hankin, J. P. Gaebler, D. Francois, A. Chernoguzov, D. Lucchetti, N. C. Brown, T. M. Gatterman, S. K. Halit, K. Gilmore, J. A. Gerber, B. Neyenhuis, D. Hayes, and R. P. Stutz, *Realization of real-time fault-tolerant quantum error correction*, Phys. Rev. X **11**, 041058 (2021).

[9] G. Semeghini, H. Levine, A. Keesling, S. Ebadi, T. T. Wang, D. Bluvstein, R. Verresen, H. Pichler, M. Kalinowski, R. Samajdar, A. Omran, S. Sachdev, A. Vishwanath, M. Greiner, V. Vuletić, and M. D. Lukin, *Probing topological spin liquids on a programmable quantum simulator*, Science **374**, 1242 (2021).

[10] S. Weber, R. Bai, N. Makki, J. Mögerle, T. Lahaye, A. Browaeys, M. Daghofer, N. Lang, and H. P. Büchler, *Experimentally accessible scheme for a fractional Chern insulator in Rydberg atoms*, arXiv:2202.00699.

[11] J. C. Hoke *et al.*, *Quantum information phases in space-time: Measurement-induced entanglement and teleportation on a noisy quantum processor*, arXiv:2303.04792.

[12] M. Iqbal, N. Tantivasadakarn, R. Verresen, S. L. Campbell, J. M. Dreiling, C. Figgatt, J. P. Gaebler, J. Johansen, M. Mills, S. A. Moses, J. M. Pino, A. Ransford, M. Rowe, P. Siegfried, R. P. Stutz, M. Foss-Feig, A. Vishwanath, and H. Dreyer, *Creation of non-Abelian topological order and anyons on a trapped-ion processor*, arXiv:2305.03766.

[13] M. Iqbal, N. Tantivasadakarn, T. M. Gatterman, J. A. Gerber, K. Gilmore, D. Gresh, A. Hankin, N. Hewitt, C. V. Horst, M. Matheny, T. Mengle, B. Neyenhuis, A. Vishwanath, M. Foss-Feig, R. Verresen, and H. Dreyer, *Topological order from measurements and feed-forward on a trapped ion quantum computer*, arXiv:2302.01917.

[14] M. Foss-Feig, A. Tikku, T.-C. Lu, K. Mayer, M. Iqbal, T. M. Gatterman, J. A. Gerber, K. Gilmore, D. Gresh, A. Hankin, N. Hewitt, C. V. Horst, M. Matheny, T. Mengle, B. Neyenhuis, H. Dreyer, D. Hayes, T. H. Hsieh, and I. H. Kim, *Experimental demonstration of the advantage of adaptive quantum circuits*, arXiv:2302.03029.

[15] C. Noel, P. Niroula, D. Zhu, A. Risinger, L. Egan, D. Biswas, M. Cetina, A. V. Gorshkov, M. J. Gullans, D. A. Huse, and C. Monroe, *Measurement-induced quantum phases realized in a trapped-ion quantum computer*, Nat. Phys. **18**, 760 (2022).

[16] E. Chertkov, Z. Cheng, A. C. Potter, S. Gopalakrishnan, T. M. Gatterman, J. A. Gerber, K. Gilmore, D. Gresh, A. Hall, A. Hankin, M. Matheny, T. Mengle, D. Hayes, B. Neyenhuis, R. Stutz, and M. Foss-Feig, *Characterizing a*

non-equilibrium phase transition on a quantum computer, arXiv:2209.12889.

[17] M. P. Fisher, V. Khemani, A. Nahum, and S. Vijay, *Random quantum circuits*, Annu. Rev. Condens. Matter Phys. **14**, 335 (2023).

[18] X. Turkeshi, R. Fazio, and M. Dalmonte, *Measurement-induced criticality in (2 + 1)-dimensional hybrid quantum circuits*, Phys. Rev. B **102**, 014315 (2020).

[19] P. Sierant, M. Schirò, M. Lewenstein, and X. Turkeshi, *Measurement-induced phase transitions in (d + 1)-dimensional stabilizer circuits*, Phys. Rev. B **106**, 214316 (2022).

[20] S. Sharma, X. Turkeshi, R. Fazio, and M. Dalmonte, *Measurement-induced criticality in extended and long-range unitary circuits*, SciPost Phys. Core **5**, 023 (2022).

[21] Y. Bao, S. Choi, and E. Altman, *Theory of the phase transition in random unitary circuits with measurements*, Phys. Rev. B **101**, 104301 (2020).

[22] S. Choi, Y. Bao, X.-L. Qi, and E. Altman, *Quantum error correction in scrambling dynamics and measurement-induced phase transition*, Phys. Rev. Lett. **125**, 030505 (2020).

[23] M. Block, Y. Bao, S. Choi, E. Altman, and N. Y. Yao, *Measurement-induced transition in long-range interacting quantum circuits*, Phys. Rev. Lett. **128**, 010604 (2022).

[24] Z. Weinstein, Y. Bao, and E. Altman, *Measurement-induced power-law negativity in an open monitored quantum circuit*, Phys. Rev. Lett. **129**, 080501 (2022).

[25] Y. Li, X. Chen, and M. P. A. Fisher, *Quantum Zeno effect and the many-body entanglement transition*, Phys. Rev. B **98**, 205136 (2018).

[26] Y. Li, X. Chen, and M. P. A. Fisher, *Measurement-driven entanglement transition in hybrid quantum circuits*, Phys. Rev. B **100**, 134306 (2019).

[27] Y. Li, X. Chen, A. W. W. Ludwig, and M. P. A. Fisher, *Conformal invariance and quantum nonlocality in critical hybrid circuits*, Phys. Rev. B **104**, 104305 (2021).

[28] Y. Li and M. P. A. Fisher, *Statistical mechanics of quantum error correcting codes*, Phys. Rev. B **103**, 104306 (2021).

[29] Y. Li, S. Vijay, and M. P. A. Fisher, *Entanglement domain walls in monitored quantum circuits and the directed polymer in a random environment*, PRX Quantum **4**, 010331 (2023).

[30] Z.-C. Yang, Y. Li, M. P. A. Fisher, and X. Chen, *Entanglement phase transitions in random stabilizer tensor networks*, Phys. Rev. B **105**, 104306 (2022).

[31] Y. Li, R. Vasseur, M. P. A. Fisher, and A. W. W. Ludwig, *Statistical mechanics model for Clifford random tensor networks and monitored quantum circuits*, arXiv:2110.02988.

[32] S. Sang, Y. Li, T. Zhou, X. Chen, T. H. Hsieh, and M. P. A. Fisher, *Entanglement negativity at measurement-induced criticality*, PRX Quantum **2**, 030313 (2021).

[33] M. J. Gullans and D. A. Huse, *Dynamical purification phase transition induced by quantum measurements*, Phys. Rev. X **10**, 041020 (2020).

[34] M. J. Gullans and D. A. Huse, *Scalable probes of measurement-induced criticality*, Phys. Rev. Lett. **125**, 070606 (2020).

[35] H. Oshima and Y. Fuji, *Charge fluctuation and charge-resolved entanglement in a monitored quantum circuit with U(1) symmetry*, Phys. Rev. B **107**, 014308 (2023).

[36] C.-M. Jian, Y.-Z. You, R. Vasseur, and A. W. W. Ludwig, *Measurement-induced criticality in random quantum circuits*, Phys. Rev. B **101**, 104302 (2020).

[37] C.-M. Jian, B. Bauer, A. Keselman, and A. W. W. Ludwig, *Criticality and entanglement in nonunitary quantum circuits and tensor networks of noninteracting fermions*, Phys. Rev. B **106**, 134206 (2022).

[38] C.-M. Jian, H. Shapourian, B. Bauer, and A. W. W. Ludwig, *Measurement-induced entanglement transitions in quantum circuits of non-interacting fermions: Born-rule versus forced measurements*, arXiv:2302.09094.

[39] J. Iaconis, A. Lucas, and X. Chen, *Measurement-induced phase transitions in quantum automaton circuits*, Phys. Rev. B **102**, 224311 (2020).

[40] J. Iaconis and X. Chen, *Multifractality in nonunitary random dynamics*, Phys. Rev. B **104**, 214307 (2021).

[41] A. Altland, M. Buchhold, S. Diehl, and T. Micklitz, *Dynamics of measured many-body quantum chaotic systems*, Phys. Rev. Res. **4**, L022066 (2022).

[42] Y. Minoguchi, P. Rabl, and M. Buchhold, *Continuous Gaussian measurements of the free boson CFT: A model for exactly solvable and detectable measurement-induced dynamics*, SciPost Phys. **12**, 009 (2022).

[43] T. Müller, S. Diehl, and M. Buchhold, *Measurement-induced dark state phase transitions in long-ranged fermion systems*, Phys. Rev. Lett. **128**, 010605 (2022).

[44] M. Buchhold, Y. Minoguchi, A. Altland, and S. Diehl, *Effective theory for the measurement-induced phase transition of Dirac fermions*, Phys. Rev. X **11**, 041004 (2021).

[45] O. Alberton, M. Buchhold, and S. Diehl, *Entanglement transition in a monitored free-fermion chain: From extended criticality to area law*, Phys. Rev. Lett. **126**, 170602 (2021).

[46] M. Buchhold, T. Müller, and S. Diehl, *Revealing measurement-induced phase transitions by pre-selection*, arXiv:2208.10506.

[47] P. Zhang, *Information scrambling and entanglement dynamics of complex Brownian Sachdev-Ye-Kitaev models*, J. High Energy Phys. 04 (2023) 105.

[48] T.-G. Zhou, Y.-N. Zhou, and P. Zhang, *Full counting statistics across the entanglement phase transition of non-Hermitian Hamiltonians with charge conservation*, Phys. Rev. B **108**, 094308 (2023).

[49] X. Turkeshi, A. Biella, R. Fazio, M. Dalmonte, and M. Schiró, *Measurement-induced entanglement transitions in the quantum Ising chain: From infinite to zero clicks*, Phys. Rev. B **103**, 224210 (2021).

[50] P. Sierant, G. Chiriacò, F. M. Surace, S. Sharma, X. Turkeshi, M. Dalmonte, R. Fazio, and G. Pagano, *Dissipative Floquet dynamics: From steady state to measurement induced criticality in trapped-ion chains*, Quantum **6**, 638 (2022).

[51] X. Turkeshi, M. Dalmonte, R. Fazio, and M. Schirò, *Entanglement transitions from stochastic resetting of non-Hermitian quasiparticles*, Phys. Rev. B **105**, L241114 (2022).

[52] A. Biella and M. Schiró, *Many-body quantum Zeno effect and measurement-induced subradiance transition*, Quantum **5**, 528 (2021).
[53] X. Turkeshi, L. Piroli, and M. Schiró, *Enhanced entanglement negativity in boundary-driven monitored fermionic chains*, Phys. Rev. B **106**, 024304 (2022).
[54] Y. L. Gal, X. Turkeshi, and M. Schirò, *Volume-to-area law entanglement transition in a non-Hermitian free fermionic chain*, SciPost Phys. **14**, 138 (2023).
[55] H. P. Casagrande, B. Xing, M. Dalmonte, A. Rodriguez, V. Balachandran, and D. Poletti, *Complexity of spin configurations dynamics due to unitary evolution and periodic projective measurements*, Phys. Rev. E **108**, 044128 (2023).
[56] Y. Fuji and Y. Ashida, *Measurement-induced quantum criticality under continuous monitoring*, Phys. Rev. B **102**, 054302 (2020).
[57] S.-K. Jian, C. Liu, X. Chen, B. Swingle, and P. Zhang, *Measurement-induced phase transition in the monitored Sachdev-Ye-Kitaev model*, Phys. Rev. Lett. **127**, 140601 (2021).
[58] M. Ippoliti, M. J. Gullans, S. Gopalakrishnan, D. A. Huse, and V. Khemani, *Entanglement phase transitions in measurement-only dynamics*, Phys. Rev. X **11**, 011030 (2021).
[59] N. Lang and H. P. Büchler, *Entanglement transition in the projective transverse field Ising model*, Phys. Rev. B **102**, 094204 (2020).
[60] A. Sriram, T. Rakovszky, V. Khemani, and M. Ippoliti, *Topology, criticality, and dynamically generated qubits in a stochastic measurement-only Kitaev model*, Phys. Rev. B **108**, 094304 (2023).
[61] G.-Y. Zhu, N. Tantivasadakarn, and S. Trebst, *Structured volume-law entanglement in an interacting, monitored Majorana spin liquid*, arXiv:2303.17627.
[62] Y. Li and M. P. A. Fisher, *Robust decoding in monitored dynamics of open quantum systems with Z_2 symmetry*, arXiv:2108.04274.
[63] J. Hauser, Y. Li, S. Vijay, and M. P. A. Fisher, *Continuous symmetry breaking in adaptive quantum dynamics*, arXiv:2304.13198.
[64] V. Sharma, C.-M. Jian, and E. J. Mueller, *Subsystem symmetry, spin glass order, and criticality from random measurements in a two-dimensional Bacon-Shor circuit*, Phys. Rev. B **108**, 024205 (2023).
[65] G.-Y. Zhu, N. Tantivasadakarn, A. Vishwanath, S. Trebst, and R. Verresen, *Nishimori's cat: Stable long-range entanglement from finite-depth unitaries and weak measurements*, arXiv:2208.11136.
[66] T.-C. Lu, L. A. Lessa, I. H. Kim, and T. H. Hsieh, *Measurement as a shortcut to long-range entangled quantum matter*, PRX Quantum **3**, 040337 (2022).
[67] N. Tantivasadakarn, R. Thorngren, A. Vishwanath, and R. Verresen, *Long-range entanglement from measuring symmetry-protected topological phases*, arXiv:2112.01519.
[68] Y. Bao, M. Block, and E. Altman, *Finite time teleportation phase transition in random quantum circuits*, arXiv:2110.06963.
[69] B. Nienhuis, *Analytical calculation of two leading exponents of the dilute Potts model*, J. Phys. A **15**, 199 (1982).
[70] B. Nienhuis, *Exact critical point and critical exponents of $O(n)$ models in two dimensions*, Phys. Rev. Lett. **49**, 1062 (1982).
[71] F. Y. Wu, *The Potts model*, Rev. Mod. Phys. **54**, 235 (1982).
[72] B. Duplantier and H. Saleur, *Exact tricritical exponents for polymers at the FTHETA point in two dimensions*, Phys. Rev. Lett. **59**, 539 (1987).
[73] P. Flory, *Principles of Polymer Chemistry*, Baker lectures 1948 (Cornell University, Ithaca, 1953).
[74] M. Fixman, *Excluded volume in polymer chains*, J. Chem. Phys. **23**, 1656 (1955).
[75] P. de Gennes, *Exponents for the excluded volume problem as derived by the Wilson method*, Phys. Lett. A **38**, 339 (1972).
[76] A. McKane, *Reformulation of $n \to 0$ models using anticommuting scalar fields*, Phys. Lett. A **76**, 22 (1980).
[77] C. Candu, J. L. Jacobsen, N. Read, and H. Saleur, *Universality classes of dense polymers and conformal sigma models*, arXiv:0908.1081.
[78] T. Kibble and N. Turok, *Self-intersection of cosmic strings*, Phys. Lett. B **116**, 141 (1982).
[79] T. Vachaspati and A. Vilenkin, *Formation and evolution of cosmic strings*, Phys. Rev. D **30**, 2036 (1984).
[80] R. J. Scherrer and J. A. Frieman, *Cosmic strings as random walks*, Phys. Rev. D **33**, 3556 (1986).
[81] M. Hindmarsh and K. Strobl, *Statistical properties of strings*, Nucl. Phys. **B437**, 471 (1995).
[82] K. Strobl and M. Hindmarsh, *Universality and critical phenomena in string defect statistics*, Phys. Rev. E **55**, 1120 (1997).
[83] A. W. Sandvik, *Stochastic series expansion method with operator-loop update*, Phys. Rev. B **59**, R14157 (1999).
[84] A. W. Sandvik and H. G. Evertz, *Loop updates for variational and projector quantum Monte Carlo simulations in the valence-bond basis*, Phys. Rev. B **82**, 024407 (2010).
[85] J. T. Chalker and P. D. Coddington, *Percolationquantum tunnelling and the integer Hall effect*, J. Phys. C **21**, 2665 (1988).
[86] J. Cardy, *Linking numbers for self-avoiding loops and percolation: Application to the spin quantum Hall transition*, Phys. Rev. Lett. **84**, 3507 (2000).
[87] J. T. Chalker, M. Ortuño, and A. M. Somoza, *Spin quantum Hall effect and plateau transitions in multilayer network models*, Phys. Rev. B **83**, 115317 (2011).
[88] Y. Ikhlef, P. Fendley, and J. Cardy, *Integrable modification of the critical Chalker-Coddington network model*, Phys. Rev. B **84**, 144201 (2011).
[89] R. Vasseur, *Logarithmic correlations in quantum Hall plateau transitions*, Phys. Rev. B **92**, 014205 (2015).
[90] L. D. C. Jaubert, M. Haque, and R. Moessner, *Analysis of a fully packed loop model arising in a magnetic Coulomb phase*, Phys. Rev. Lett. **107**, 177202 (2011).
[91] A. F. Albuquerque, F. Alet, and R. Moessner, *Coexistence of long-range and algebraic correlations for short-range valence-bond wave functions in three dimensions*, Phys. Rev. Lett. **109**, 147204 (2012).
[92] A. Nahum, J. T. Chalker, P. Serna, M. Ortuño, and A. M. Somoza, *Deconfined quantum criticality, scaling*

violations, and classical loop models, Phys. Rev. X **5**, 041048 (2015).

[93] A. Nahum, P. Serna, J. T. Chalker, M. Ortuño, and A. M. Somoza, *Emergent so(5) symmetry at the Néel to valence-bond-solid transition*, Phys. Rev. Lett. **115**, 267203 (2015).

[94] J. D'Emidio and R. K. Kaul, *First-order superfluid to valence-bond solid phase transitions in easy-plane* $\mathrm{SU}(n)$ *magnets for small n*, Phys. Rev. B **93**, 054406 (2016).

[95] P. Fendley, *Topological order from quantum loops and nets*, Ann. Phys. (Amsterdam) **323**, 3113 (2008).

[96] P. Fendley and V. Krushkal, *Tutte chromatic identities from the Temperley-Lieb algebra*, Geomet. Topol. **13**, 709 (2009).

[97] P. Fendley and V. Krushkal, *Link invariants, the chromatic polynomial and the Potts model*, Adv. Theor. Math. Phys. **14**, 507 (2010).

[98] M. A. Levin and X.-G. Wen, *String-net condensation: A physical mechanism for topological phases*, Phys. Rev. B **71**, 045110 (2005).

[99] Z. Dai and A. Nahum, *Quantum criticality of loops with topologically constrained dynamics*, Phys. Rev. Res. **2**, 033051 (2020).

[100] A. Nahum, P. Serna, A. M. Somoza, and M. Ortuño, *Loop models with crossings*, Phys. Rev. B **87**, 184204 (2013).

[101] A. Nahum, J. T. Chalker, P. Serna, M. Ortuño, and A. M. Somoza, *Phase transitions in three-dimensional loop models and the* CP^{n-1} *sigma model*, Phys. Rev. B **88**, 134411 (2013).

[102] A. Nahum, J. T. Chalker, P. Serna, M. Ortuño, and A. M. Somoza, *Length distributions in loop soups*, Phys. Rev. Lett. **111**, 100601 (2013).

[103] A. Nahum, *Universality class of the two-dimensional polymer collapse transition*, Phys. Rev. E **93**, 052502 (2016).

[104] A. Nahum, J. Ruhman, S. Vijay, and J. Haah, *Quantum entanglement growth under random unitary dynamics*, Phys. Rev. X **7**, 031016 (2017).

[105] P. Fendley, *Loop models and their critical points*, J. Phys. A **39**, 15445 (2006).

[106] P. Fendley and J. L. Jacobsen, *Critical points in coupled Potts models and critical phases in coupled loop models*, J. Phys. A **41**, 215001 (2008).

[107] P. A. Pearce and J. Rasmussen, *Solvable critical dense polymers*, J. Stat. Mech. (2007) P02015.

[108] E. Vernier, J. L. Jacobsen, and H. Saleur, *Dilute oriented loop models*, J. Phys. A **49**, 064002 (2016).

[109] S. Sang and T. H. Hsieh, *Measurement-protected quantum phases*, Phys. Rev. Res. **3**, 023200 (2021).

[110] A. Nahum and B. Skinner, *Entanglement and dynamics of diffusion-annihilation processes with Majorana defects*, Phys. Rev. Res. **2**, 023288 (2020).

[111] J. Merritt and L. Fidkowski, *Entanglement transitions with free fermions*, Phys. Rev. B **107**, 064303 (2023).

[112] J. L. Jacobsen, N. Read, and H. Saleur, *Dense loops, supersymmetry, and Goldstone phases in two dimensions*, Phys. Rev. Lett. **90**, 090601 (2003).

[113] M. Fava, L. Piroli, T. Swann, D. Bernard, and A. Nahum, *Nonlinear sigma models for monitored dynamics of free fermions*, arXiv:2302.12820 [Phys. Rev. X (to be published)].

[114] H. Saleur, *New exact exponents for two-dimensional self-avoiding walks*, J. Phys. A **19**, L807 (1986).

[115] M. J. Martins, B. Nienhuis, and R. Rietman, *Intersecting loop model as a solvable super spin chain*, Phys. Rev. Lett. **81**, 504 (1998).

[116] J. Cardy, *Crossing formulae for critical percolation in an annulus*, J. Phys. A **35**, L565 (2002).

[117] C. Candu and H. Saleur, *A lattice approach to the conformal* $\mathrm{OSp}(2S+2|2S)$ *supercoset sigma model. Part I: Algebraic structures in the spin chain. The Brauer algebra*, Nucl. Phys. **B808**, 441 (2009).

[118] P. Martin, *Potts Models and Related Problems in Statistical Mechanics* (World Scientific, Singapore, 1991).

[119] In particular, loops with fugacity $n = 1$ can be described by the $\mathrm{SO}(4)_1$ representation of the BMW algebra.

[120] J. S. Birman and H. Wenzl, *Braids, link polynomials and a new algebra*, Trans. Am. Math. Soc. **313**, 249 (1989).

[121] J. Murakami, *The Kauffman polynomial of links and representation theory*, Osaka J. Math. **24**, 745 (1987).

[122] D. Fattal, T. S. Cubitt, Y. Yamamoto, S. Bravyi, and I. L. Chuang, *Entanglement in the stabilizer formalism*, arXiv:0406168.

[123] S. Aaronson and D. Gottesman, *Improved simulation of stabilizer circuits*, Phys. Rev. A **70**, 052328 (2004).

[124] D. Gottesman, *The Heisenberg representation of quantum computers*, arXiv:quant-ph/9807006.

[125] This should not be confused for the total length of the loop through the whole spacetime bulk, as considered in Ref. [100].

[126] J. L. Jacobsen and H. Saleur, *Exact valence bond entanglement entropy and probability distribution in the XXX spin chain and the Potts model*, Phys. Rev. Lett. **100**, 087205 (2008).

[127] Please note that we work in units of log(2) so that entropies reflect exactly the integer number of loops.

[128] The mutual information $I_2(A,B)$ is uniquely characterized by the ensemble average of $\sum_{l\in A}\sum_{m\in B}|\langle\gamma_l(T)\gamma_m(T)\rangle|$.

[129] A. Lavasani, Y. Alavirad, and M. Barkeshli, *Measurement-induced topological entanglement transitions in symmetric random quantum circuits*, Nat. Phys. **17**, 342 (2021).

[130] K. Klocke and M. Buchhold, *Topological order and entanglement dynamics in the measurement-only XZZX quantum code*, Phys. Rev. B **106**, 104307 (2022).

[131] As a minimal example, consider the four-qubit stabilizer state with stabilizer generator $\mathcal{G} = \langle\gamma_1\gamma_5, \gamma_2\gamma_3, \gamma_4\gamma_8, \gamma_6\gamma_7\rangle$. After a Jordan-Wigner transformation, we have $\mathcal{G} = \langle X_1X_2, Y_1Z_2X_3, X_3X_4, X_2Z_3Y_4\rangle$ in the clipped gauge. Consider now taking subsystems A, B, and C to be qubits 1, 2, and 4, respectively. Whereas $I_2(B,C) = 1$ from the fermionic loop representation, in the spin-qubit language we have $I_2(B,C) = 0$. As a result, the tripartite mutual information $I_3(A,B,C)$ is nonvanishing in the spin language, while it is necessarily zero in the fermionic loop language. The origin of this difference lies in the nonlocal nature of the Jordan-Wigner transformation. Stabilizers with end points in disconnected regions such as B and C still have nontrivial operator weight in the intervening region due to the Jordan-Wigner string.

[132] D. Bulgakova and O. Ogievetsky, *Fusion procedure for the walled Brauer algebra*, J. Geom. Phys. **149**, 103580 (2020).
[133] G. Benkart, M. Chakrabarti, T. Halverson, R. Leduc, C. Lee, and J. Stroomer, *Tensor product representations of general linear groups and their connections with Brauer algebras*, J. Algebra **166**, 529 (1994).
[134] R. J. Baxter, *Exactly Solved Models in Statistical Mechanics* (Academic, New York, 1982).
[135] Y. Imamura, *Construction of the Temperley-Lieb algebra from bond algebra: From the transverse-field Ising to the XXZ*, arXiv:2203.14545.
[136] Or, alternatively, by a supersymmetric formulation on an enlarged space $\mathbb{CP}^{m|m}$ with $m \in \mathbb{Z}_+$ [77].
[137] S. J. Elman, A. Chapman, and S. T. Flammia, *Free fermions behind the disguise*, Commun. Math. Phys. **388**, 969 (2021).
[138] K. G. Wilson and M. E. Fisher, *Critical exponents in 3.99 dimensions*, Phys. Rev. Lett. **28**, 240 (1972).
[139] R. K. P. Zia and D. J. Wallace, *Critical behaviour of the continuous n-component Potts model*, J. Phys. A **8**, 1495 (1975).
[140] D. J. Amit, *Renormalization of the Potts model*, J. Phys. A **9**, 1441 (1976).
[141] V. Dotsenko, J. L. Jacobsen, M.-A. Lewis, and M. Picco, *Coupled Potts models: Self-duality and fixed point structure*, Nucl. Phys. **B546**, 505 (1999).
[142] S. B. Bravyi and A. Y. Kitaev, *Fermionic quantum computation*, Ann. Phys. (Amsterdam) **298**, 210 (2002).
[143] F. Roser, H. P. Büchler, and N. Lang, *Decoding the projective transverse field Ising model*, Phys. Rev. B **107**, 214201 (2023).
[144] This can be made more apparent by a unitary transformation $\prod_l e^{-i\pi X_{2l-1}X_{2l}/4}$: It maps the circuit to a variant of the cluster model [129], whereas here XZX and Z are measured with equal probabilities.
[145] S. Murciano, P. Sala, Y. Liu, R. S. K. Mong, and J. Alicea, *Measurement-altered Ising quantum criticality*, arXiv:2302.04325.
[146] E. J. Beamond, A. L. Owczarek, and J. Cardy, *Quantum and classical localization and the Manhattan lattice*, J. Phys. A **36**, 10251 (2003).
[147] Y. Bao, S. Choi, and E. Altman, *Symmetry enriched phases of quantum circuits*, Ann. Phys. (Amsterdam) **435**, 168618 (2021).
[148] G. Delfino and E. Tartaglia, *Classifying Potts critical lines*, Phys. Rev. E **96**, 042137 (2017).
[149] B. Duplantier, *Two-dimensional fractal geometry, critical phenomena and conformal invariance*, Phys. Rep. **184**, 229 (1989).
[150] W. Janke and A. M. Schakel, *Geometrical vs. Fortuin-Kasteleyn clusters in the two-dimensional q-state Potts model*, Nucl. Phys. **B700**, 385 (2004).
[151] B. Nienhuis, A. N. Berker, E. K. Riedel, and M. Schick, *First- and second-order phase transitions in Potts models: Renormalization-group solution*, Phys. Rev. Lett. **43**, 737 (1979).
[152] F. Y. Wu, *Dilute Potts model, duality and site-bond percolation*, J. Phys. A **14**, L39 (1981).
[153] A. Coniglio and F. Peruggi, *Clusters and droplets in the q-state Potts model*, J. Phys. A **15**, 1873 (1982).
[154] Y. M. M. Knops, H. W. J. Blote, and B. Nienhuis, *Multicriticality in a self-dual Potts model*, J. Phys. A **26**, 495 (1993).
[155] J. L. Cardy, *Conformal invariance and surface critical behavior*, Nucl. Phys. **B240**, 514 (1984).
[156] C.-J. Lin, W. Ye, Y. Zou, S. Sang, and T. H. Hsieh, *Probing sign structure using measurement-induced entanglement*, Quantum **7**, 910 (2023).
[157] F. C. Alcaraz, *Order of phase transition for systems with multispin interactions: Monte Carlo simulations*, Phys. Rev. B **34**, 4885 (1986).
[158] K. A. Penson, R. Jullien, and P. Pfeuty, *Phase transitions in systems with multispin interactions*, Phys. Rev. B **26**, 6334 (1982).
[159] A. Milsted, L. Seabra, I. C. Fulga, C. W. J. Beenakker, and E. Cobanera, *Statistical translation invariance protects a topological insulator from interactions*, Phys. Rev. B **92**, 085139 (2015).
[160] A. Rahmani, X. Zhu, M. Franz, and I. Affleck, *Emergent supersymmetry from strongly interacting Majorana zero modes*, Phys. Rev. Lett. **115**, 166401 (2015).
[161] A. Rahmani, X. Zhu, M. Franz, and I. Affleck, *Phase diagram of the interacting Majorana chain model*, Phys. Rev. B **92**, 235123 (2015).
[162] H. Blöte, A. Compagner, P. Cornelissen, A. Hoogland, F. Mallezie, and C. Vanderzande, *Critical behaviour of two Ising models with multispin interactions*, Physica (Amsterdam) **139A**, 395 (1986).
[163] W. Selke, *The ANNNI model—Theoretical analysis and experimental application*, Phys. Rep. **170**, 213 (1988).
[164] L. Turban, *One-dimensional Ising model with multispin interactions*, J. Phys. A **49**, 355002 (2016).
[165] E. O'Brien and P. Fendley, *Lattice supersymmetry and order-disorder coexistence in the tricritical Ising model*, Phys. Rev. Lett. **120**, 206403 (2018).
[166] A. Zabalo, M. J. Gullans, J. H. Wilson, S. Gopalakrishnan, D. A. Huse, and J. H. Pixley, *Critical properties of the measurement-induced transition in random quantum circuits*, Phys. Rev. B **101**, 060301(R) (2020).
[167] H. Lóio, A. D. Luca, J. D. Nardis, and X. Turkeshi, *Purification timescales in monitored fermions*, Phys. Rev. B **108**, L020306 (2023).
[168] The phase diagram of this model was previously obtained in Ref. [58]. However, no logarithmic correction was observed for the considered system sizes.
[169] M. Ippoliti and V. Khemani, *Postselection-free entanglement dynamics via spacetime duality*, Phys. Rev. Lett. **126**, 060501 (2021).
[170] T.-C. Lu and T. Grover, *Spacetime duality between localization transitions and measurement-induced transitions*, PRX Quantum **2**, 040319 (2021).
[171] M. Ippoliti, T. Rakovszky, and V. Khemani, *Fractal, logarithmic, and volume-law entangled nonthermal steady states via spacetime duality*, Phys. Rev. X **12**, 011045 (2022).
[172] I. Reid and B. Bertini, *Entanglement barriers in dual-unitary circuits*, Phys. Rev. B **104**, 014301 (2021).

[173] T. Prosen, *Many-body quantum chaos and dual-unitarity round-a-face*, Chaos **31**, 093101 (2021).
[174] C. Jonay, V. Khemani, and M. Ippoliti, *Triunitary quantum circuits*, Phys. Rev. Res. **3**, 043046 (2021).
[175] P. W. Claeys and A. Lamacraft, *Emergent quantum state designs and biunitarity in dual-unitary circuit dynamics*, Quantum **6**, 738 (2022).
[176] Y. Kasim and T. Prosen, *Dual unitary circuits in random geometries*, J. Phys. A **56**, 025003 (2023).
[177] P. W. Claeys, M. Henry, J. Vicary, and A. Lamacraft, *Exact dynamics in dual-unitary quantum circuits with projective measurements*, Phys. Rev. Res. **4**, 043212 (2022).
[178] A. Foligno and B. Bertini, *Growth of entanglement of generic states under dual-unitary dynamics*, Phys. Rev. B **107**, 174311 (2023).
[179] D. T. Stephen, W. W. Ho, T.-C. Wei, R. Raussendorf, and R. Verresen, *Universal measurement-based quantum computation in a one-dimensional architecture enabled by dual-unitary circuits*, arXiv:2209.06191.
[180] M. A. Rampp, R. Moessner, and P. W. Claeys, *From dual unitarity to generic quantum operator spreading*, Phys. Rev. Lett. **130**, 130402 (2023).
[181] P. W. Claeys, A. Lamacraft, and J. Vicary, *From dual-unitary to biunitary: A 2-categorical model for exactly-solvable many-body quantum dynamics*, arXiv:2302.07280.
[182] G. M. Sommers, D. A. Huse, and M. J. Gullans, *Crystalline quantum circuits*, PRX Quantum **4**, 030313 (2023).
[183] J. M. Koh, S.-N. Sun, M. Motta, and A. J. Minnich, *Measurement-induced entanglement phase transition on a superconducting quantum processor with mid-circuit readout*, Nat. Phys. **19**, 1314 (2023).
[184] J. P. Bonilla Ataides, D. K. Tuckett, S. D. Bartlett, S. T. Flammia, and B. J. Brown, *The XZZX surface code*, Nat. Commun. **12**, 2172 (2021).
[185] R. Morral-Yepes, F. Pollmann, and I. Lovas, *Detecting and stabilizing measurement-induced symmetry-protected topological phases in generalized cluster models*, arXiv:2302.14551.
[186] R. Verresen, R. Moessner, and F. Pollmann, *One-dimensional symmetry protected topological phases and their transitions*, Phys. Rev. B **96**, 165124 (2017).
[187] S. Trebst, P. Werner, M. Troyer, K. Shtengel, and C. Nayak, *Breakdown of a topological phase: Quantum phase transition in a loop gas model with tension*, Phys. Rev. Lett. **98**, 070602 (2007).
[188] A. Lavasani, Z.-X. Luo, and S. Vijay, *Monitored quantum dynamics and the Kitaev spin liquid*, Phys. Rev. B **108**, 115135 (2023).